

Improving Thermal Stability of Perovskite Solar Cells by Suppressing Ion Migration using Copolymer Grain Encapsulation

Y. Zhou, C. Nam

To be published in "Chemistry of Materials"

July 2021

Center for Functional Nanomaterials
Brookhaven National Laboratory

U.S. Department of Energy
USDOE Office of Science (SC), Basic Energy Sciences (BES) (SC-22)

Notice: This manuscript has been authored by employees of Brookhaven Science Associates, LLC under Contract No. DE-SC0012704 with the U.S. Department of Energy. The publisher by accepting the manuscript for publication acknowledges that the United States Government retains a non-exclusive, paid-up, irrevocable, world-wide license to publish or reproduce the published form of this manuscript, or allow others to do so, for United States Government purposes.

DISCLAIMER

This report was prepared as an account of work sponsored by an agency of the United States Government. Neither the United States Government nor any agency thereof, nor any of their employees, nor any of their contractors, subcontractors, or their employees, makes any warranty, express or implied, or assumes any legal liability or responsibility for the accuracy, completeness, or any third party's use or the results of such use of any information, apparatus, product, or process disclosed, or represents that its use would not infringe privately owned rights. Reference herein to any specific commercial product, process, or service by trade name, trademark, manufacturer, or otherwise, does not necessarily constitute or imply its endorsement, recommendation, or favoring by the United States Government or any agency thereof or its contractors or subcontractors. The views and opinions of authors expressed herein do not necessarily state or reflect those of the United States Government or any agency thereof.

Improving Thermal Stability of Perovskite Solar Cells by Suppressing Ion Migration using Copolymer Grain Encapsulation

Yuchen Zhou,^{1,†} Yifan Yin,^{1,†} Xianghao Zuo,¹ Likun Wang,¹ Tai-De Li,² Yuan Xue,¹
Ashwanth Subramanian,¹ Yiwei Fang,¹ Yichen Guo,¹ Zhenhua Yang,¹ Mircea Cotlet,³
Chang-Yong Nam,^{1,3,*} and Miriam H. Rafailovich^{1,*}

¹Department of Materials Science and Chemical Engineering, Stony Brook University,
Stony Brook, NY 11794, USA.

²Advanced Science Research Center at the Graduate Center of the City University of
New York, NY 10031, USA.

³Center for Functional Nanomaterials, Brookhaven National Laboratory, Upton, NY
11973, USA.

† These authors contributed equally.

* Corresponding authors: cynam@bnl.gov (C.-Y.N.),
miriam.rafailovich@stonybrook.edu (M.H.R.)

Abstract

Thermal stability of organic-inorganic hybrid perovskites (OIHPs) remains as one of the critical challenges against the stable operation of perovskite solar cells (PSCs) in direct sunlight with elevated temperatures. Here, we show an addition of polystyrene-co-polyacrylonitrile (SAN) copolymer can significantly enhance thermal stability of OIHPs and improve the stability of the corresponding PSCs by suppressing migration of organic cations in OIHP. The methylammonium lead iodide (MAPI) with SAN incorporated within the perovskite layer featured a superior thermal stability compared to pure MAPI without SAN, only displaying average 5-15% decrease in PCE even after continuous thermal aging for 24 h at 100 °C. The secondary ion mass spectrometry revealed that the thermal degradation of the pure MAPI was largely associated with MA⁺ out-migration. Conducting atomic force microscopy analysis further indicated the incorporated SAN led to a suppression of ionic currents present at the grain boundaries of the perovskite film, which was understood by high immiscibility between SAN and MA⁺ components as confirmed by the experimentally estimated Flory-Huggins parameter between them. This study newly identifies a promising potential of using polymer grain encapsulation for enhancing thermal stability of OIHPs and their solar cell performance by suppressing the out-diffusion of cationic organic components.

Introduction

Perovskite solar cells (PSCs), based on organic-inorganic halide perovskite (OIHP) materials, have been an area of intensive research since 2009,¹ due to their good photovoltaic (PV) performance and high power conversion efficiency (PCE).² Despite their excellent optoelectronic characteristics, the OIHPs and their PSCs still suffer from poor performance stability. Extensive efforts have been paid to improve the overall stability of the OIHPs and PSCs in the last few years, and improved encapsulation technologies have proven effective in protecting the devices from moisture induced degradation.³⁻⁶ Thermal stability is, however, still one of the major concerns in today's PSCs and is primarily responsible for the quick degradation of the OIHP structures. Specifically, during a conventional operation under continuous illumination, protective encapsulations cannot mitigate the degradation induced by light and accumulated heat,⁷ as significant ion migration still occurs, degrading the OIHP as well as the device interfaces.⁸⁻¹¹ Furthermore, encapsulation technologies provide additional complications when considering a roll-to-roll manufacturing process.

Among the types of OIHPs used in making PSCs, methylammonium lead iodide ($\text{CH}_3\text{NH}_3\text{PbI}_3$ or MAPbI_3 or MAPI) perovskite is one of the most classic OIHPs,¹²⁻¹⁵ because of its great optoelectronic properties, such as high absorption coefficient, wide absorption range, low exciton binding energy, long electron and hole diffusion lengths, high ambipolar charge mobilities, and extended charge carrier lifetime.¹⁶ However, it is known that the MAPI perovskite might have poorer thermal stability than other types of OIHPs.¹⁷⁻¹⁹ A complete decomposition of MAPI

phase into non-photoactive and insulating PbI_2 can take as short as minutes when exposed in high temperature even in an inert atmosphere.¹⁸ Compositionally, the fast decomposition might result from the depletion of mobile MA^+ species and highly volatile MA^+ based components (MAI and MA, etc) in high temperature.^{20, 21} Previous study shows that the concentration of mobile MA^+ ions is one order of magnitude higher than that of mobile I^- ions in MAPI OIHP.²² The escaping of a large concentration of volatile MA^+ components from the MAPI lattice, thus, results in the degradation of the MAPI into PbI_2 . In structural point-of-view, while the MA^+ components can possibly release from the top surface of the MAPI thin film, it is also understood that the presence of the grain boundaries (GBs) in solution-processed polycrystalline OIHP thin films can accelerate such a thermal degradation, since the GBs are also believed to be responsible for facilitating fast diffusion of ion species and molecules.²³⁻²⁵

One plausible strategy is to slow down the general mobility of the migrating cationic species through partially or even fully replacing it with one or two other types of larger, more stable cations, such as formamidinium ion (FA^+) and Cs^+ , etc.^{18, 26, 27} The mixed cationic system, sometimes with mixed halides,^{28, 29} can deliver an OIHP film with better performance and stability. This approach can, however, change the bandgap of the MAPI and complicate the processing of the film, as a recent study showed that a faster degradation of cations occurs in the precursor solution during the storage when mixed cations of Cs^+ , FA^+ , and MA^+ , and halides of Br^- and I^- are used,^{30, 31} even if protected from direct lighting.³¹ Thus, a freshly made solution is usually required for a good quality, mixed OIHP thin film,

potentially negatively affecting the processing cost in a practical manufacturing setting. Another method focuses on reducing the GB densities by increasing the grain size of the MAPI OIHPs by optimizing device processing conditions, such as using solvent mixtures or different spin casting protocols.^{12, 32, 33} Even though these methods reported the production of larger grains with improved performance, the thermal stability at high temperature (100 °C or above) are rarely reported, since the highly volatile MA⁺ species are still able to diffuse easily through the untreated GBs at elevated temperatures.

Numerous approaches, including surface coating,³⁴⁻³⁷ antisolvent dripping^{38,}³⁹ as well as directly mixing with the precursors,⁴⁰⁻⁴⁴ have been reported for passivating the perovskite surface and/or GBs. Also reported were the addition of nanomaterials such as PCBM,³⁸ carbon nanotube⁴⁵ and graphene/graphene oxide,⁴⁶ , small molecule ligands including 2-aminoethanethiol (AET)⁴⁷ and terephthalic acid (TPA),³⁹ as well as long chain polymers such as poly(methyl methacrylate) (PMMA)⁴⁸, poly(vinyl pyridine) (PVP),⁴⁹ polyurethane (PU),⁴⁴ poly(vinyl alcohol) (PVA),⁵⁰ poly[N-9'-heptadecanyl-2,7-carbazole-alt-5,5-(4',7'-di-2-thienyl-2',1',3'-benzothiadiazole)] (PCDTBT),⁵¹ polycaprolactone (PCL)⁴⁰ and block copolymers of poly(ethylene oxide) (PEO) and poly(phenylene oxide) (PPO)⁴².

For example, Lin et al.⁴⁵ recently introduced single-wall carbon nanotubes, functionalized with 'nano-tweezer'-like organic surfactant, to passivate the MAPI perovskite GBs. They reported increased charge mobility and an overall improvement in performance and operational stability, but without addressing the thermal stability. Hou et al.³⁹ incorporated an organic ligand additive, TPA, onto the

MAPI perovskite film, via the antisolvent dripping. This process was shown to passivate the defects at the GBs and grain surfaces, resulting in increased PV performance and moisture stability after storage in a relative humidity of 30%. The impact on the thermal stability though was not so good, and the PCE of the device based on TPA modified perovskite still dropped to ~50% of its initial value when aged at 100 °C for 24 h. Wang et al.⁴¹ experimented with adding a macromolecular additive, the F127 Pluronic copolymer, to passivate an FA⁺/MA⁺ mixed perovskite and demonstrated enhanced performance and increased ambient (moisture) and operational stability, which they attributed to GB passivation. Significantly, in contrast to previous studies, they also reported a promising thermal stability, even though they only reported the aging of half cells at 120 °C for 1h. Overall, these prior studies highlight a research need for developing strategies that can specifically address the thermal stability issue of PSCs to enable a practical operation and application of PSCs in direct sunlight conditions with elevated temperature.

In this paper, we present a new, copolymer-based additive approach for improving the thermal stability of MAPI perovskite and PSCs and propose a new mechanism to explain the observed stability enhancement. Particularly, we select to study the effect of addition of a random copolymer of polystyrene-*co*-polyacrylonitrile. This choice of polymer is rationalized considering its higher glass transition temperature (T_g : ~117 °C) than regular polystyrene, which would provide chain flexibility during thermal exposure but would unlikely diffuse fully out of the perovskite matrix. Two processing techniques for introducing the polymer using the chlorobenzene were compared, i.e., surface coating and drip-incorporation, where

the latter was able to achieve as high as 95% preservation of the device PCE on average after 24 h of aging at 100 °C. The microstructure evolution of the MAPI perovskite with and without the polymer was analyzed, using electron microscopy in conjunction with the complementary techniques of contact angle goniometry, time of flight secondary ion mass spectroscopy (ToF-SIMS), as well as conducting atomic force microscopy (c-AFM), in order to understand the correlation between the enhanced thermal stability and the influence of the polymer on the internal structure and the ion migration associated with the GBs.

Experimental Section

Materials

Polystyrene-*co*-polyacrylonitrile (SAN) random copolymer, Lustran 31 UNL, with 31% acrylonitrile (molecular weight (M_w): 169,000 Da) was purchased from Bayer Polymers. Lead iodide (PbI_2 , 99.99% trace metal basis) was purchased from TCI Co. Ltd. All other materials, including fluorine doped tin oxide (FTO) glass (TEC 7), methylammonium iodide (MAI, anhydrous, 99%), dimethylformamide (DMF, anhydrous, 99.8%), dimethyl sulfoxide (DMSO, anhydrous, 99.9%), chlorobenzene (CB, anhydrous, 99.8%), and 2,2',7,7'-tetrakis[N,N-di(4-methoxyphenyl)amino]-9,9'-spirobifluorene (Spiro-OMeTAD) were purchased from Sigma-Aldrich. All chemicals were used as received without further purification.

Fabrication of perovskite solar cells

The FTO glass substrates were consecutively washed using 2% Hellmanex aqueous solution, deionized water and ethanol in the sonication bath. After drying with nitrogen, the substrates were cleaned by ultraviolet (UV)-ozone treatment for 10 min. A compact TiO_2 (c- TiO_2) layer was then deposited on the cleaned FTO glass substrates via spin-casting of its precursor solution, followed by sol-gel reaction at 450 °C, as reported previously. On top of the c- TiO_2 coated substrates, a mesoscopic TiO_2 (meso- TiO_2) layer was deposited by spin coating the diluted solution of the TiO_2 paste (mass ratio of paste: ethanol = 1:6) at 4500 rpm for 10 s with a ramp speed of 3000 rpm/s, followed by the baking at 500 °C for 20 min. To prepare the MAPI perovskite thin film with or without incorporated SAN polymer, the MAPI precursor solution was firstly prepared by dissolving

equal molar of MAI and PbI₂ (1.2 M) in the mixed solvents consisting of 90% DMF and 10% DMSO. The perovskite layers were then deposited onto the m-TiO₂/c-TiO₂/FTO substrates by spin casting at 4000 rpm for 30 s.

SAN solutions were first prepared by dissolving 0.1, 0.5, and 1 mg/ml of SAN in CB. Two methods were used to introduce the SAN copolymer to the MAPI perovskite. We refer to the first approach as “incorporated” in this manuscript, where the incorporation of SAN polymer was achieved during the antisolvent dripping step. The CB solution containing different concentrations of SAN were dripped onto the substrates 10 s after the start of the spin coating process. The as-cast perovskite was then annealed on a hotplate at 100 °C for 10 min to form a shining dark brown perovskite layer. For the other method, which is referred to as “surface-coated”, the SAN polymer solutions of 0.5 and 1.0 mg/ml were spun cast onto the as-prepared pristine MAPI thin film at 4000 rpm for 30 s, followed by annealing at 100 °C for 10 min. This method produced a thin polymer layer coating on top of the perovskite film. The average thickness of the layers corresponding to the two solutions are, 1.9 and 2.8 nm, respectively, as determined by the ellipsometry on films spun cast from the two solutions on single crystal (100) polished Si wafers.

The hole transport layer (HTL) was prepared by first dissolving 80 mg Spiro-OMeTAD in 1 ml chlorobenzene together with 20 µL of 500 mg/mL stock solution of lithium bis(trifluoromethanesulfonyl)imide (LiTFSI) in acetonitrile and 30 µL of 4-tert-butylpyridine (tBP), followed by the spin casting the solution on top of the perovskite layer at 4000 rpm for 30 s. Finally, 80 nm thick Au electrodes were deposited by physical vapor deposition. All the procedures, except for the electrode deposition, were completed in an Ar-filled glove box.

Structure characterization

The crystal structures of the formed perovskite films were characterized using the X-ray diffractometry (XRD, Rigaku Ultima III) with a sampling step of 0.04° . The perovskite surface morphologies were mainly characterized using scanning electron microscopy (SEM, Hitachi S-4800) at the 3 kV acceleration voltage. The water contact angle on different perovskite films were extracted using the CAM 200 Optical Goniometer. Lateral force scanning microscopy (Bruker Dimension 3000) in contact mode was used to measure the friction variation on the sample surface. Optical absorption spectra of the perovskite films on quartz glass substrates were measured using a UV-visible spectrophotometer (Cary 60, Agilent, USA) in the wavelength range of 400 nm to 800 nm. Steady-state and time-resolved photoluminescence (PL) experiments were performed using the time-correlated single photon counting spectroscopy by exciting the perovskite thin film deposited on quartz coated substrates at the wavelength of 450 nm.

Photovoltaic performance measurements

The PV performance of the PSCs was measured on a modified PV probe station. The simulated illumination with an air mass 1.5 global (AM1.5G) filter was generated by a 150 W solar simulator (Oriel, 96000) with an around 3 cm-diameter uniform illumination area. The light intensity of $100 \text{ mW}\cdot\text{cm}^{-2}$ (1 sun) was calibrated using a calibrated Si solar cell (Oriel) before the measurements. The current density-voltage (J-V) measurements were carried out on PSCs with the substrate size of $1.5 \text{ cm} \times 1.5 \text{ cm}$ and an active area of 0.0314 cm^2 under illumination at a scan rate of 50 mV/s between -0.02 V and 1.2 V for both reverse and forward scans. We note that the choice of J-V scan rate generally can

affect the measured performance of PSCs and hysteresis. The use of an identical scan rate for all devices in the current study enables a direct comparison of device performances induced by the addition of polymer additive. Steady-state PCE measurements were conducted by tracking the photocurrent of the biased PSCs (at the voltage corresponding to the maximum power point) under 1 sun illumination. External quantum efficiency (EQE) measurements were carried out using a home-built EQE setup composed of a 300 W xenon lamp (Oriel) and a monochromator (Oriel) attached to the PV probe station. All above measurements were performed in open air.

Thermal stability measurements

To measure the stability of the perovskites (with and without SAN polymer), several half-cells, which consist of the perovskite layer/m-TiO₂/c-TiO₂/FTO, were first prepared. The prepared half-cells were then thermally aged at 100 °C in a dark and Ar-filled atmosphere for as long as 24 h. The changes of the crystal structure as well as morphology after certain period of aging were characterized using XRD and SEM, respectively. The performance stability of PSCs was also conducted based on the thermally aged half-cells. After certain periods of aging, certain aged half-cells were cooled down and brought to the spin coater for depositing Spiro-OMETAD from the freshly made solution. Then, top Au electrode was deposited by physical vapor deposition. For each J-V measurement, new Spiro-OMETAD and Au electrode layers were deposited on the aged half-cells to eliminate the impact of degradation in the HTL and electrode/HTL interfaces.

Measurements of ion distribution and migration

The depth profile of ions, especially MA^+ , in HTL coated perovskite half-cell before and after thermal aging were measured using ToF-SIMS (PHI TRIFT V nano ToF-SIMS). The depth profiles of positive ions (e.g., C^+ , MA^+ , Pb^+ , and Ti^+ , etc) were constructed by sputtering the samples using 5 keV Ar gas gun (50 nA current, rastered over $800 \mu\text{m} \times 800 \mu\text{m}$ area) and in sequence probing the composition of the exposed surface by using a 30 keV Bi^+ liquid metal ion beam and analyzing the sputtered secondary ions across $300 \mu\text{m} \times 300 \mu\text{m}$ area. Samples were sputtered 10 s before probing ions.

The activation energy of ion migration of the perovskite layer was measured using a variable-temperature probe station (MMR Technologies) under vacuum (~ 1 mTorr). Two-terminal devices with in-plane electrodes were fabricated for measurements by depositing the perovskites films on a quartz coated substrate, followed by depositing two top lateral Au electrodes with the channel length of $50 \mu\text{m}$ and channel width of 1mm using a shadow mask. During the measurement, the device was first stabilized at each target temperature for 10 min. The temperature-dependent current (I) was then recorded by biasing the device at 5 V with a corresponding electrical field of $0.1 \text{ V}/\mu\text{m}$.

Results

Microstructures of the MAPI perovskites with surface-coated and incorporated SAN polymer

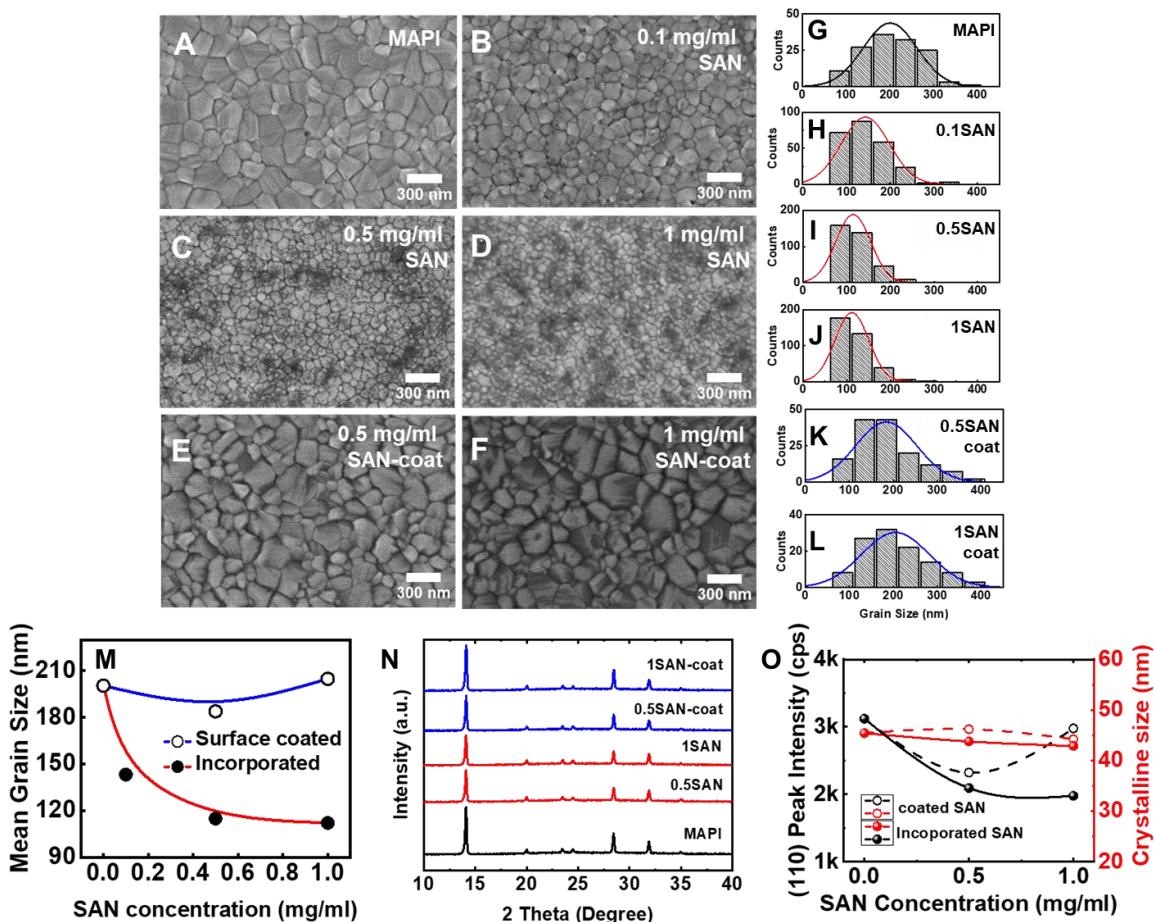


Figure 1. Morphology and crystallinity of the MAPI perovskite with SAN polymer. Top-view SEM micrographs of: (A) pristine, (B) 0.1 mg/ml, (C) 0.5 mg/ml, and (D) 1 mg/ml SAN-incorporated, as well as (E) 0.5 mg/ml, and (F) 1 mg/ml SAN-surface-coated MAPI films, with (G-L) showing corresponding MAPI grain size distributions with respect to the concentrations of incorporated (red) and surface-coated (blue) SAN. (M) Comparison of SAN-concentration-dependent MAPI grain size variation between SAN surface coating (blue) and direct incorporation (red). (N) XRD spectra of the MAPI perovskite with SAN (blue and red) and without SAN (black). (O) Comparisons of SAN-concentration-dependent variations of (110) peak intensity (black) and crystalline size (red) in MAPI between SAN surface coating (hollow) and direct incorporation (solid).

The surface morphologies of the SAN-perovskite films produced by the two methods were determined by SEM as shown in Figure 1A-F. All films with and without

SAN polymer exhibit relatively smooth surfaces with compact grains fully covering the substrates. The corresponding grain size distribution is calculated from the SEM micrograph and plotted in Figure 1G-L. The mean grain size, plotted in Figure 1M as a function of SAN concentration for both the incorporated and coated methods, shows that the direct surface coating method has nearly no influence on grain size, which is consistent to the fact that perovskite grains are first formed before the application of the SAN coating. In contrast, incorporating the SAN polymer into the perovskite has a pronounced effect on the grain size (Figure 1M), where the average grain size decreases from ~200 nm to ~100 nm as the concentration of SAN in the antisolvent dripping solution is increased. Furthermore, within a sample, the grain size becomes more uniform as can be seen from the narrowing of the distribution in the histograms shown in Figure 1G-J. In this case, the SAN polymer acts as a heterogeneous nucleation site for the MAPI crystallites. The increase in SAN concentration effectively increases the number of nuclei (i.e., nucleation rate) and, thus, decreases the mean size of the perovskite grains due to a lowered growth rate. The data confirms the incorporation of SAN by the dripping method is a more effective way to introduce the SAN polymer into the bulk interior of the MAPI perovskite thin film.

In Figure 1N, we show XRD spectra obtained from the perovskite thin films. The crystalline structures exhibit the typical MAPI perovskite tetragonal structure for all samples, suggesting that both SAN application methods do not affect the crystal phases or introduce impurities into the perovskite layer. The intensity of the (110) peak as well as the corresponding crystallite size determined by the Debye-Scherrer analysis of the full width at half maximum (FWHM) of the peak, are plotted as a function of SAN concentration for

both methods (Figure 1O). The data clearly indicates that the intensity of the peak, which reflects the extent of crystallinity, follows closely the trends of the mean grain sizes determined from the SEM images (Figure 1A-L). We have previously shown that the apparent grains of MAPI films observed in SEM are composed of smaller crystallites with different orientations and slightly mismatched boundaries.⁴⁰ The crystallite size determined by XRD is around 45 nm regardless of the polymer concentration (Figure 1O), which is consistently smaller than the apparent grain size seen in SEM. This implies that the crystallite size and, thus, crystallinity of perovskite are unaffected by the constraints imposed on the size of apparent grains by increasing SAN polymer concentration.

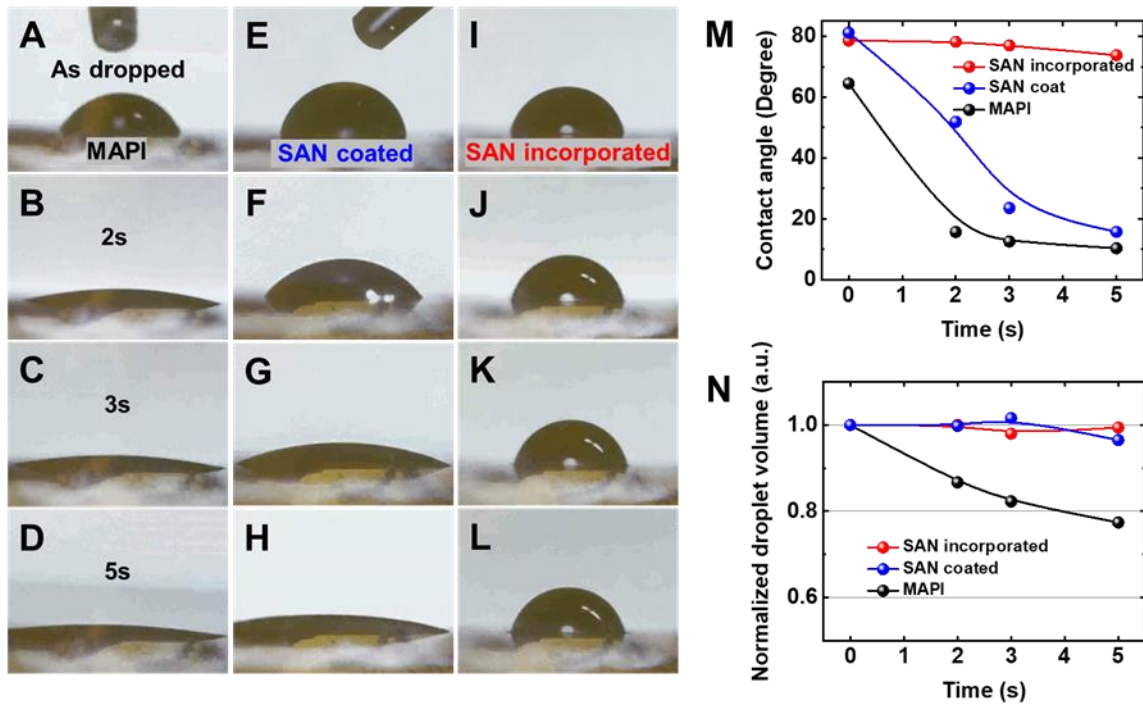


Figure 2. (A-L) Optical micrographs of water droplets being dropped on MAPI thin films: (A-D) pristine, (E-H) SAN-surface-coated, and (I-L) SAN-incorporated MAPI. (M) Temporal evolution of the corresponding droplet contact angles on pristine (black), SAN-surface-coated (blue), and SAN-incorporated (red) MAPI films. (N) Temporal evolution of the droplets volume on pristine (black), SAN-surface coated (blue), and SAN-incorporated (red) MAPI films.

We further probed the effects of distribution of SAN polymer in the MAPI perovskite by using contact angle goniometry and AFM. Figure 2A-D show time-lapse optical micrographs of a deionized water droplet placed on the surface of the pristine MAPI perovskite film. As shown in Figure 2M, the contact angle rapidly drops from the initial 64.5° to 15.7° in as short as 2 s and continues to drop asymptotically in the next 3 s, reaching a plateau at approximately 10.4° after 5 s. As further discussed in a later section, there is a roughly ~ 10 nm thick organic MA^+ rich layer formed on the surface of the MAPI film, and this is responsible for the observed rapid wetting of water as the MA^+ rich layer can be rapidly displaced by water. Meanwhile, on the surface of SAN-coated perovskite, the initial water contact angle is as large as 81.2° (Figure 2E, M) but still reduces to 51.9° in 2 s and eventually to 15.8° in 5 s (Figure 2F-H, M). The initially large contact angle can be explained by the 2.8 nm thick SAN layer covering the perovskite film as noted previously. This SAN layer thickness, however, is much smaller than the radius of gyration (R_g ; 15.7 nm) for SAN (M_w 169,000 Da), indicating the polymer chains in the layer are most likely in a highly stretched configuration which has a strong tendency to de-wet^{52, 53}, thus explaining the eventual decrease of water contact angle after 5 s as the SAN layer is displaced by water. In a drastic contrast, when a water droplet is placed on the MAPI film with the incorporated SAN, the initially large contact angle (78.6°) remains mostly unchanged, decreasing only to 73.8° even after 5 s (Figure 2I-L, M). This suggests that the surface coating from the incorporated SAN is stable to the hydration, which is most likely due to the encapsulation of the grain (surface and GBs) by SAN polymer occurring during the perovskite crystal growth.⁴³ The increased stability to degradation from hydration (moisture) by the incorporation of SAN is also consistent with previous observations,

which explained that the phenomenon was due to sequestration of the polymer within the GBs.^{40, 42, 54} The notion that the SAN encapsulation of grains improves the stability of perovskite in moisture is further supported by the dynamics of the droplet volumes on the three types of surfaces, as shown in Figure 2N. On the pristine MAPI surface, the volume of the droplet decreases by more than 20% within the first 5 s, which is much faster than the natural evaporation rate. In this case, the water is rapidly wicked via the GBs into the interior of the films. In the case of the MAPI films with either coated or incorporated SAN polymer, the volume of the water droplet is generally stable, indicating that the polymer is presenting on both surfaces, hindering the wicking process. We note that the effective protection against moisture ingress by SAN is likely associated with its major hydrophobic polystyrene block, constituting 69% of M_w .

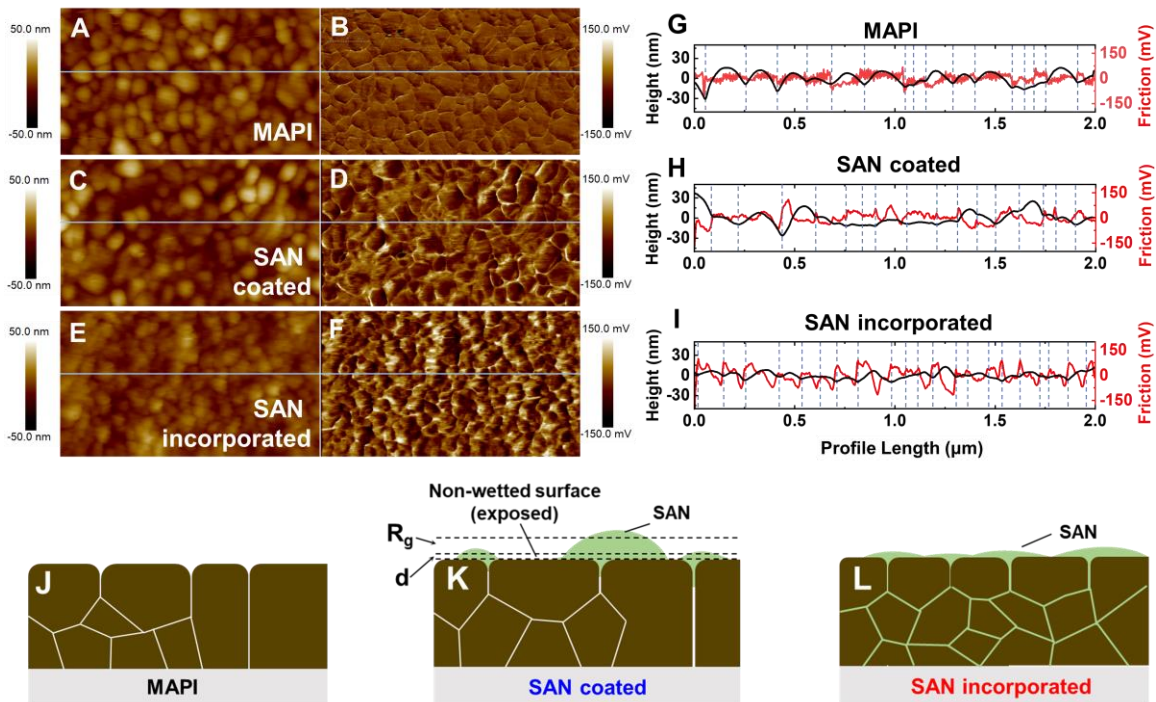


Figure 3. Effects of SAN passivation methods (surface coating and direct incorporating) on surface morphology of MAPI perovskites. (A, C, and E) AFM surface height and (B, D, and F) corresponding lateral force (friction) images of the pristine (A and B), SAN-surface-coated (C and D), and SAN-incorporated (E and F) MAPI perovskites. (G, H, and I) Line plots of Height (nm) and Friction (mV) versus Profile Length (μm) for MAPI, SAN coated, and SAN incorporated, respectively. (J, K, and L) Schematic diagrams of the surface morphology for MAPI, SAN coated, and SAN incorporated, respectively. Panel K shows a 'Non-wetted surface (exposed)' and labels ' R_g ' and ' d '.

D), and SAN-incorporated (E and F) MAPI films. (G-I) Height and lateral force (friction) profiles corresponding to the marked lines in A-F, respectively. The blue dashes indicate the GB areas. (J-L) Schematic models illustrating the SAN polymer distributions on SAN-surface-coated and SAN-incorporated MAPI films. R_g and d represent radius of gyration and average thickness of coated SAN, respectively.

Topography and the corresponding AFM lateral force (friction) images obtained from the pristine, SAN-surface-coated, and SAN-incorporated MAPI films are shown in Figure 3A-F. The data were analyzed from a series of line profiles (Figure 3G-I), such as those shown in the respective figures. The blue dashes on the profiles indicate the positions of GBs determined from the height profiles. For the pristine MAPI film, topography images indicate the surface roughness of 8.4 nm, corresponding to the average height of the grains, which can also be seen from Figure 3G. The lateral force scan, which is sensitive to the type of materials being probed, is on the other hand remarkably flat and featureless, consistent to the fact that the interior of each grain and the GBs are both composed of MAPI perovskite (Figure 3G). Meanwhile, the roughness of the topographical scan of the SAN-coated sample is ~9.8 nm (Figure 3C), which lies between distinctively rough and smooth areas with roughness of 11.0 nm (at 0 – 0.6 μm in the profile) and 6.0 nm (at 0.6 – 1.3 μm in the profile), respectively (Figure 3H). This is consistent with the non-uniform coating of the SAN layer as noted earlier. The lateral force image (Figure 3D) reveals a soft region with higher friction (at 0.6 – 1.3 μm) surrounded by lower-friction regions (at 0 – 0.6 μm and 1.3 – 2 μm) in Figure 3H, which indicates a concentration of softer material, i.e., SAN polymer, along the GBs. The topographically flatter regions (at 0.6 – 1.3 μm) also appear to have overall higher friction regardless of grain structure (Figure 3H), indicating these regions are also covered with the polymer layer. In contrast, the topographical images of the SAN-incorporated MAPI film display flatter line profiles and, thus, lower roughness, consistent to a thin polymer layer uniformly covering the entire

surface (Figure 3E,I). The lateral force scanning image (Figure 3F) also features a highly uniform line profile (Figure 3I) with friction peaks coinciding with the GBs, indicating the passivation of GBs with a thicker polymer.

The combined results from the contact angle and AFM measurements lead to a model for the distribution of the SAN copolymer in MAPI film as illustrated in Figure 3J-L. The pristine MAPI films without the polymer are composed of a series of flat compact grains, separated by untreated GBs (Figure 3J). Deposition of SAN onto the MAPI films *via* spin casting produces a thin, but unstable and non-uniform coating, which dewets easily and only partially passivates the GBs (Figure 3K). Application of the same amount of SAN *via* antisolvent dripping incorporates the polymer into the MAPI polycrystalline grain structure as reported before,^{38, 39} not only covering the grain surface but also providing a uniform passivation of GBs (Figure 3L).

Optical properties of the MAPI perovskites with surface-coated and incorporated SAN

The optical absorption and the steady-state PL measurements further revealed the effect of the SAN polymer on the radiative recombination characteristics of the photo-excited charge carriers in the MAPI thin film. For a meaningful comparison, the amount of optical absorption in the pristine, SAN-surface-coated, and SAN-incorporated films were kept nearly identical by using nearly identical film thicknesses as evidenced by similar optical absorption spectra (Figure 4A). Despite the identical optical absorption, the PL emission spectra displayed drastically different peak intensities at around 775 nm depending on the sample condition (Figure 4A). Among the three samples, the SAN-incorporated film exhibits the highest PL intensity, while the pristine perovskite film shows

the lowest and the perovskite with surface-coated SAN polymer presents an intermediate intensity (Figure 4A). The PL spectral shape and onset wavelength however remain nearly identical among the three conditions, indicating that the SAN polymer, either surface-coated or incorporated, does not affect the optical bandgap of MAPI perovskites. The results confirm that the non-radiative recombination associated with the defects and traps in the perovskite surface and GBs has been overall reduced by the addition of SAN polymer, especially to a greater extent when SAN was directly incorporated within the perovskite, uniformly passivating the perovskite surface and GBs.

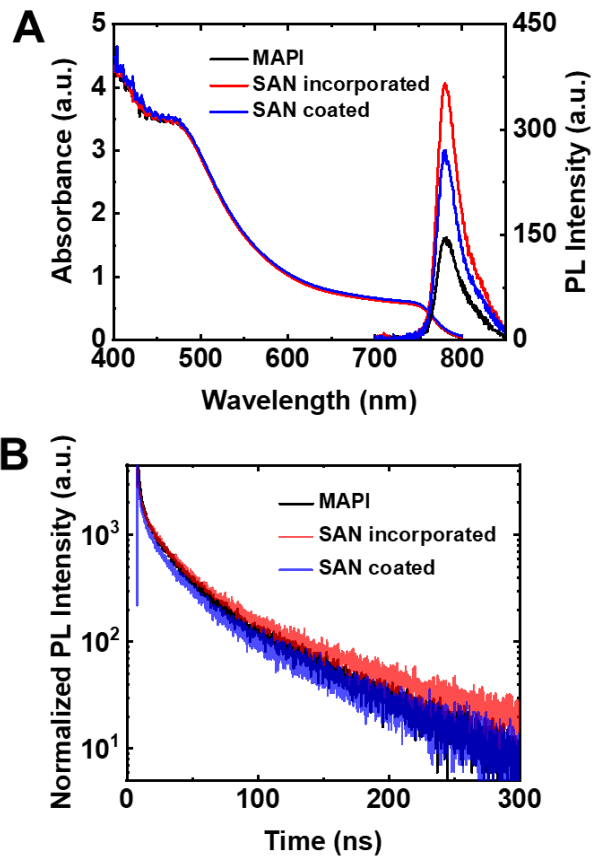


Figure 4. Optical properties of the pristine (black), SAN-surface-coated (blue), and SAN-incorporated (red) MAPI perovskites. (A) UV–visible optical absorption and steady-state PL spectra. (B) Temporal PL intensity decay profiles.

The recombination dynamics of photo-excited charge carriers were further examined by the time-resolved PL measurement (Figure 4B). The temporal PL decay characteristics of the pristine, SAN-surface-coated, and SAN-incorporated films were analyzed by the bi-exponential decay model with fast and slow time constants (τ_1 and τ_2 , respectively). We find that the average lifetime (τ_{avg}) for the pristine perovskite was 44.8 ns with the fast and slow decay time at 11.5 and 64.8 ns, respectively. With surface coated SAN, τ_{avg} become slightly longer (47.4 ns) with corresponding τ_1 and τ_2 increasing to 13.9 and 71.5 ns, respectively. The perovskite with incorporated SAN polymer exhibited the longest τ_{avg} (61.9 ns) with τ_1 and τ_2 of 17.5 and 96.5 ns, respectively (Table S1). The faster decay component ($\tau_1 < 20$ ns) is generally attributed to the trapping of charge carriers in defect states, while the slower decay components ($\tau_2 > 20$ ns) is largely related to the direct bimolecular radiative recombination in the bulk.^{55, 56} The PL lifetime data suggest fewer defects and traps in the bulk of the perovskite when the SAN additive was directly incorporated into the MAPI layer, whereas the surface coating of SAN introduced only a marginal improvement. Consistent to the steady-state PL data, the longer PL lifetime of the polymer-incorporated perovskite indicates the presence of fewer mobile defects and traps due to the encapsulation of the perovskite grains and the associated passivation of the GBs and the perovskite film surface. Overall, the incorporation of SAN polymer in MAPI perovskite leads to improved optoelectronic properties of the perovskite, while the spin coated SAN layer only provides partial passivation of the perovskite surface.

The influence on the PV performance by addition of SAN copolymer

The comparison of PV performance of the as-prepared perovskite with and without SAN polymer shows that the application of SAN not only improves the device PCE but

also reduces the J-V hysteresis. We used an ‘p-i-n’ PSC structure consisting of Au/Spiro-OMeTAD/MAPI (with or without SAN)/m-TiO₂/c-TiO₂/FTO, from top to bottom (see the Experimental Section for details). Representative illuminated J-V characteristics reveal that the control MAPI PSCs without SAN has PCEs of 17.25% from the reverse scan with short circuit current density (J_{SC}), open circuit voltage (V_{OC}), and fill factor (FF) of 23 mA/cm², 1.06 V, and 0.71, respectively (Figure 5A). The control device features a relatively large hysteresis index (HI) of 0.26, which was calculated by comparing the current densities at 80% of V_{OC} of its reverse and forward scans⁵⁷, despite the use of the m-TiO₂ layer. A large hysteresis generally results from severe ion migration originated from the non-passivated perovskite layer.⁵⁸

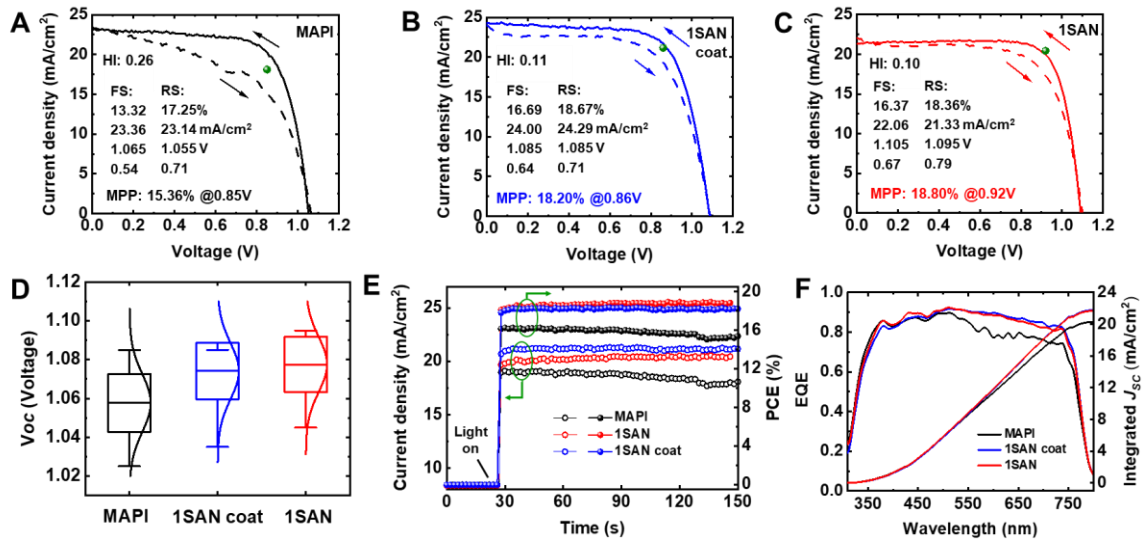


Figure 5. PV characteristics of PSCs based on pristine, SAN-surface-coated, and SAN-incorporated MAPI perovskites. Typical, forward- (dash) and reverse-scan (solid) J-V characteristics of typical best-performing (A) pristine, (B) SAN-surface-coated, and (C) SAN-incorporated MAPI PSCs. The green dots represent the actual maximum power point (MPP) extracted from the steady-state PCE measurements. (D) Statistic V_{OC} distribution, (E) steady-state PCE, as well as (F) EQE spectra with integrated J_{SC} of the PSCs based on pristine (black), SAN-surface-coated (blue), and SAN-incorporated (red) MAPI perovskites.

By coating the SAN polymer (1 mg/ml) onto the surface of perovskite, the PCE increased to 18.67% (reverse scan) due to the increase in J_{SC} and V_{OC} to 24.3 mA/cm² and

1.09 V with largely unchanged FF of 0.71, compared to the control perovskite (Figure 5B). Most notably, there is a significant decrease in HI to 0.11. Given that the SAN coating is applied on the surface of perovskite before the Spiro-OMeTAD hole transport layer (HTL), the reduced HI implicates that the J-V hysteresis is associated with the out-migration of ions from the perovskite layer to the HTL. The direct incorporation of SAN (1 mg/ml) into perovskite also leads to an increased PCE to 18.36% (reverse scan) with J_{SC} , V_{OC} , FF, and HI of 21.3 mA/cm², 1.10 V, 0.79, and 0.1, respectively (Figure 5C). The PCE is comparable to that of the surface-SAN-coated perovskite despite ~ 2 mA/cm² reduction in J_{SC} due to the 10 mV increase in V_{OC} combined with the 11% increase in FF. The average PV parameters measured from 10-15 separate PSCs for each condition consistently confirm that the directly SAN-incorporated perovskite has higher V_{OC} and FF than the surface-SAN-coated perovskite, with comparable PCE (Figure 5D, Figure S1, and Table S2). The higher V_{OC} and FF in the SAN-incorporated perovskite is consistent with its higher PL emission intensity and longer PL lifetime than the surface-SAN-coated perovskite (Figure 4), which indicates a more effective reduction in the defect-mediated non-radiative charge recombination by the direct incorporation of SAN into perovskite. The average HI of SAN-incorporated perovskite is also smaller than that of surface-SAN-coated counterpart (Figure S1D). Overall, the PV performance of as-prepared PSCs along with the observed PL characteristics strongly supports the notion that the direct incorporation of SAN into perovskite is highly effective in not only reducing the charge carrier recombination but also mitigating the ion migration in the perovskite by passivating the surface and GBs of perovskite. The overall improved PV performance by the application of SAN is also observed in the measured EQE, as the EQE is enhanced in the longer wavelength region (>

500 nm) with the SAN passivation (both surface coating and direct incorporation), compared with the control perovskite without SAN (Figure 5F), which again reflects a reduced charge carrier recombination⁵⁹ afforded by the effective passivation of charge traps in the perovskite by the SAN polymer. The integrated J_{SC} from the EQE results are 20.3, 21.8 and 21.7 mA/cm² for the pristine, surface-SAN-coated, and SAN-incorporated PSCs, respectively (Figure 5F), representing the 13%, 9% and 2% differences to the J_{SC} values extracted from the J-V (FS) curves. Although the difference in the directly measured and EQE-integrated J_{SC} can be smaller than 5% for high-performance PSC devices in literatures, the mismatch of J_{SC} by ~10% is also not uncommon in several prior publications as reviewed in a recent report.⁶⁰ While the exact origins warrant a further investigation, considering the reduced HI by the application of SAN, the smaller J_{SC} mismatch after introducing SAN polymer (especially when directly incorporated) strongly suggests that the J_{SC} mismatch is likely correlated with the ion migration in the PSC devices.⁶⁰ We note that the somewhat lower J_{SC} of SAN-incorporated perovskite compared with the surface-SAN-coated counterpart is potentially caused by the increased bulk resistivity due to the presence of insulating polymer on the surface and in the layer of the perovskite; consistently, two-terminal ohmic MAPI perovskite devices with top, in-plane lateral Au electrodes showed an increasing resistance upon incorporation of SAN (Figure S2).

The measured steady-state PCE shows that the application of SAN to perovskites enables a pronounced improvement in the operational stability of PSCs. The steady-state PCE was obtained by subjecting PSCs to the maximum power point (MPP) voltage (V_{mpp}) in illuminated J-V characteristics (AM1.5G, 1 Sun) and measuring the corresponding current density (J_{mpp}) during a continuous, AM1.5G-1 Sun illumination for 120 s. As shown

in Figure 5E, in contrast to the control perovskite without SAN featuring the reduction in J_{mpp} from 19.09 to 18.07 mA/cm² during 2 min, both the SAN-surface-coated and SAN-incorporated perovskites maintain J_{mpp} . Consequently, the PCE of SAN-incorporated perovskite stabilizes at 18.8% after 2 min illumination, which is now *higher* than that of SAN-surface-coated counterpart (18.2%). In the meantime, the PCE of control perovskite stabilizes at 15.4%. These variations of steady-state PCE under illumination are more intuitively illustrated by superimposing the 2 min-stabilized MPPs of each PSC conditions in comparison with the initial J-V traces (green dots, Figure 5A-C), which show the MPP of SAN-incorporated perovskite is located slightly outside the reverse J-V trace while those of SAN-surface-coated and control perovskites reside between the forward and reverse J-V traces, with the control significantly more so. Considering that the stabilized, steady-state PCE is regarded as a more practically meaningful figure-of-merit of solar cell performance,⁶¹ the results highlight the favorable effects of directly incorporating SAN into perovskite for improving the PV performance of PSCs. The PV performance of surface-SAN-coated and SAN-incorporated PSCs with a reduced SAN concentration (0.5 mg/ml) also exhibited similar trends as the 1 mg/ml counterparts (Figure S3 and Table S2)

Thermal stability of the MAPI perovskites and the corresponding PSCs with and without SAN

The thermal stability of polycrystalline MAPI perovskite thin film with and without SAN polymer has been evaluated by exposing the films at 100 °C for 24 h and measuring the evolution of crystal structure (Figure 6A-E) as well as morphology (Figure 6F-T) by XRD and SEM. The XRD result shows that in the pristine perovskite, the PbI₂ (001) peak at 12.5° occurs after as short as 6 h of thermal aging and becomes even more significant

after 24 h (Figure 6A). The quick increase of the amount of PbI_2 during thermal exposure indicates a relatively poor thermal stability of MA^+ -based perovskite, due to the dissociation and migration of volatile MA^+ out of the perovskite crystal lattice. A previous study⁶² showed that macroscopically, the degradation of MAPbI_3 at moderately high temperatures (76-144 °C) generally occurs through the following decomposition reaction: $\text{CH}_3\text{NH}_3\text{PbI}_3$ (MAPbI_3) \rightarrow CH_3NH_2 (g) + HI (g) + PbI_2 (s). We expect that at the elevated temperature, mobile MA^+ ions migrate through untreated GBs and react with other mobile ions, forming volatile HI and MA -component-based CH_3NH_2 and eventually leaving behind PbI_2 .

The morphological analysis using SEM (Figure 6F-H) clearly confirms the presence of nanoplatelet-type PbI_2 crystals (yellow circles) at the intergranular regions of the perovskite after 6 h of thermal aging (Figure 6G), suggesting that the degradation of the polycrystalline perovskite is initiated from the GB region and, thus, emphasizing the need of GB passivation for improved thermal structural stability. After 24 h, the perovskite film features large PbI_2 crystallites grown out of the plane thus with overall less compact film morphology (Figure 6H), which is further supported by a low-magnification SEM micrograph clearly showing the contrast between brighter PbI_2 crystallites and remaining darker perovskite regions (Figure S4).

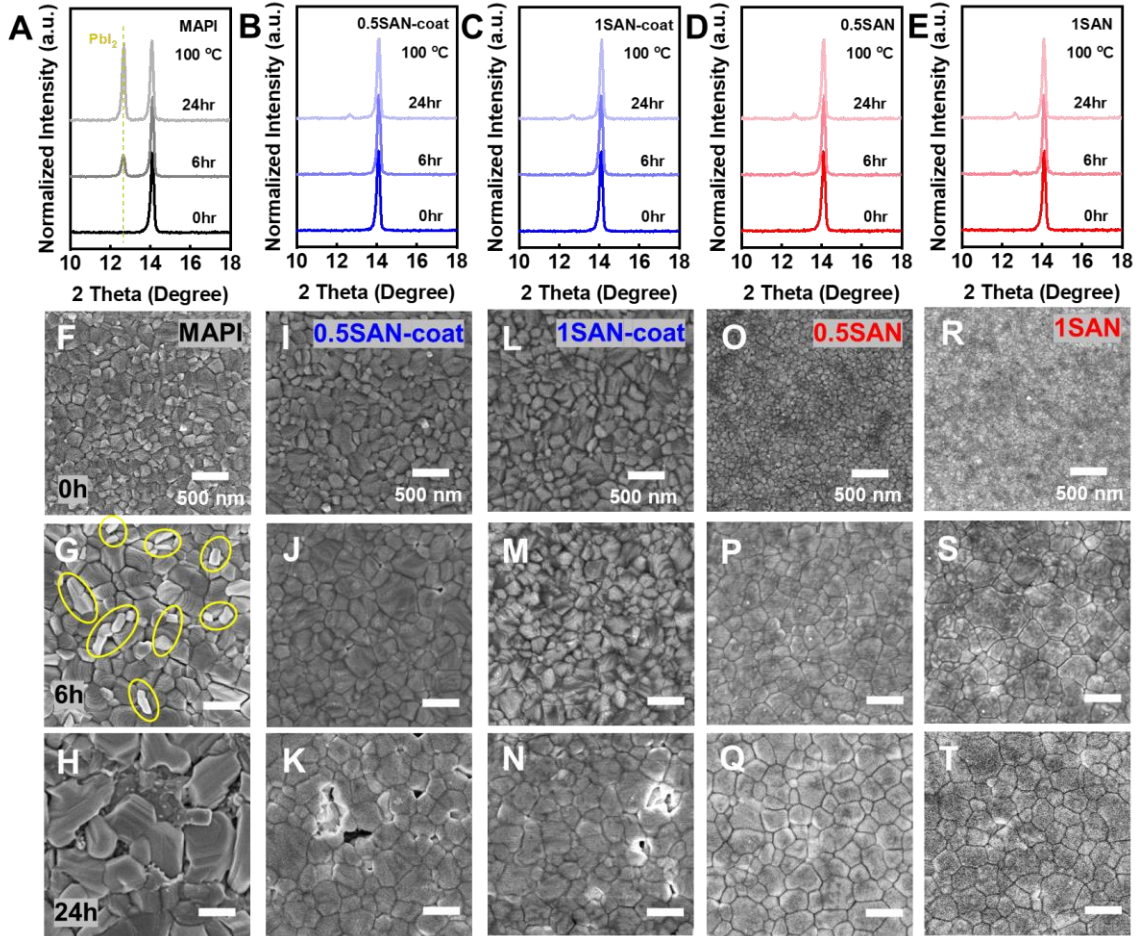


Figure 6. Structural and morphological evolution of MAPI perovskite films with and without SAN during 100 °C thermal stability test. (A-E) Crystal structure evolution and (F-T) morphological change with respect to thermal aging time of: (A, F-H) pristine, (B, I-K) 0.5 mg/ml, and (C, L-N) 1 mg/ml SAN-surface-coated, as well as (D, O-Q) 0.5 mg/ml and (E, R-T) 1 mg/ml SAN-incorporated MAPI perovskites. Yellow circles in (G) indicate the presence of PbI_2 at GBs.

On the contrary, a significantly enhanced thermal stability is witnessed in the MAPI perovskite films with surface-coated and incorporated SAN. Specifically, XRD confirms that much less amount of PbI_2 crystal is formed even after the 24 h thermal exposure, as indicated by the very small PbI_2 (001) intensity at 12.5° (Figure 6B-E), with the surface morphology observed by SEM showing no obvious formation of PbI_2 platelets (Figure 6I-T). However, cracks and holes do appear after 24 h of thermal aging in the perovskite coated with a lower concentration (0.5 mg/ml) SAN (Figure 6K). Though less severe, the perovskite coated with the higher concentration (1.0 mg/ml) SAN also feature small cracks

and pinholes (Figure 6N). It is the perovskite film with incorporated SAN that exhibits the best thermal stability; even after 24 h thermal again, the film surface features compact and smooth grain morphology without noticeable cracks or pinholes in both SAN concentrations (Figure 6Q,T). It is noted that there is growth of apparent grain sizes seen in SEM for SAN-applied perovskites as the thermal aging duration increases, which is likely driven by the fusion of neighboring grains with similar crystal orientation.^{63, 64} The observed increase in thermal stability of MAPI perovskite structure and the suppressed decomposition to PbI_2 by the application of SAN are most likely driven by the reduced out-diffusion of MA^+ from the perovskite layer. The direct incorporation of SAN into perovskites leads to the passivation of both surface and GB channels, effecting a better ability in maintaining the compositional and morphological integrity of MAPI during the thermal aging as compared with the surface-SAN-coated counterpart.

We further establish a direct correlation between the structure and properties of the thermally aged SAN-applied MAPI perovskites with their PV performance by fabricating PSCs based on thermally aged half-cells without Spiro-OMeTAD HTL and top Au electrode. This approach exclusively probes the impact of the structural variation in the MAPI layer induced by thermal aging on the PV performance by eliminating possible thermal degradation of the HTL and Au electrode.^{39, 41, 56} The half-cells, consisting of FTO bottom substrate, m-TiO₂/c-TiO₂ electron transfer layer (ETL), and perovskite with or without SAN, were first subjected to a 100 °C thermal stress in the dark, Ar-filled atmosphere for 6 h, 17 h, or 24 h. After each period of aging, a fresh Spiro-OMeTAD HTL and Au electrode were deposited on the aged half-cells right before PV performance characterization (Figure 7A).

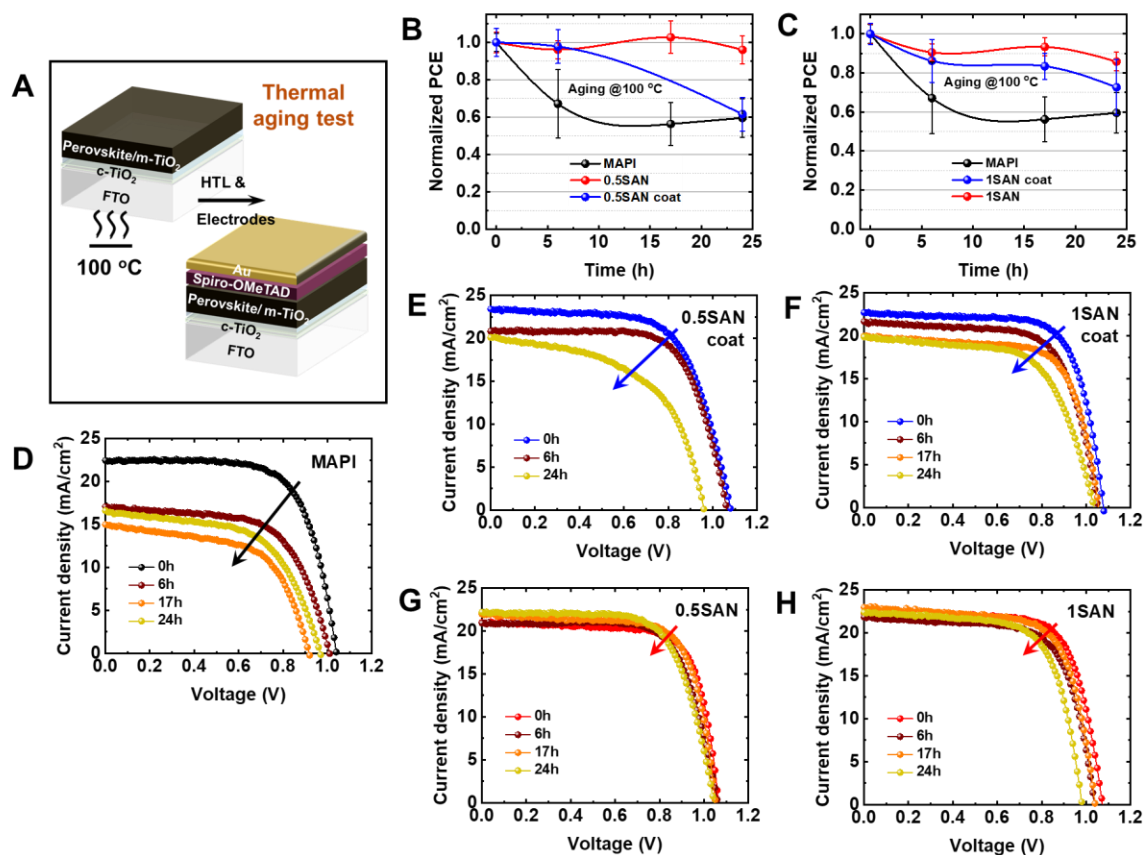


Figure 7. Thermal stability of PSCs based on MAPI perovskites with and without SAN polymer. (A) Schematics depicting the thermal stability test based on half cells. (B, C) Evolution of PCE of PSCs with SAN as a function of thermal aging time at 100 °C (in Ar atmosphere and dark) for two different SAN concentrations: 0.5 mg/ml (B), and 1 mg/ml (C), with black, blue, and red denoting pristine, SAN-surface-coated, and SAN-incorporated MAPI perovskites, respectively. Note that the solid trend curves are drawn only for guiding eyes. (D-H) Representative J-V characteristics after different aging time for PSCs based on: (D) pristine, (E) 0.5 mg/ml, (F) 1 mg/ml SAN-surface-coated, as well as (G) 0.5 mg/ml and (H) 1 mg/ml SAN-incorporated MAPI perovskites.

Consistent to the observed poor thermal stability of pristine MAPI perovskite structure, the average PCE of PSCs made of the perovskite without SAN decreased to ~70% of its initial value after only 6 h thermal aging and below 60% after 24 h (Figure 7B and C). The representative illuminated J-V characteristics of the aged PSCs feature a drastic decrease in J_{SC} accompanied by a less severe but still appreciable decrease in V_{OC} and FF (Figure 7D and Figure S5). The rapid decrease in J_{SC} after thermal aging is directly related to the decomposition of the photoactive MAPI perovskite into the insulating PbI₂, while

the reduction in FF is likely associated with an increased device interfacial resistance caused by the formation of less compact surface morphologies. The results highlight that the poor thermal stability of the MAPI perovskite structure itself plays a major role in causing the PV performance degradation under thermal aging besides potential thermal degradation of HTL and ETL.

Unlike the pristine perovskite, the PSCs based on the perovskite with surface-coated SAN (0.5 mg/ml) maintains over 95% of the initial PCE on average after the first 6 h of thermal aging at 100 °C. However, a continued thermal aging for 24 h renders the PCE only slightly higher than 60% of the initial PCE (Figure 7B) with overall decreases in J_{SC} , V_{OC} , and FF (Figure 7E), thus barely showing advantages over the control PSC without SAN (Figure 7B). If SAN is directly incorporated into the perovskite, we observe an excellent thermal stability of PV performance; the PSCs with directly incorporated SAN (0.5 mg/ml) maintain above 95% of the initial PCE even after 24 h, 100 °C aging (Figure 7B), with minor change in J_{SC} , V_{OC} , and FF (Figure 7G). The PSCs with higher SAN concentration (1 mg/ml) show a similar thermal stability improvement, with over 70% of PCE being preserved after 24 h aging for the surface-SAN-coated perovskite devices and over 85% of PCE for the SAN-incorporated ones (Figure 7C). Apparently, the thermal stability imparted by the surface SAN coating is improved by the increased SAN concentration compared with the lower concentration (0.5 mg/ml) counterpart as evidenced by the relatively less degraded J-V characteristics after 24 h (Figure 7F and Figure S5). Meanwhile, when directly incorporated in the perovskite, the increased SAN concentration was in fact not so effective as the lower concentration counterpart in improving the thermal ability of the PCE of PSCs, featuring appreciable decreases in FF and V_{OC} (Figure 7H and

S5), in spite of the well-preserved structure and morphology of MAPI. Considering the glass transition temperature (T_g) of SAN (117.4 °C; Figure S6) which is close to the thermal aging temperature and the fact that, we suspect the diffusion of SAN towards the device interfaces (e.g., top surface) during the thermal aging can occur, leading to an increased interfacial resistance, thus increasing charge recombination during transport and, subsequently, decreasing FF and V_{OC} during aging (Figure S5F). Overall, the results highlight that the direct SAN incorporation into the MAPI perovskite, which passivates both perovskite GBs and grain surfaces, is favored for enhancing the thermal stability of PCE compared with the SAN surface coating as it helps preserve the phase purity but is less ideal in preserving pinhole- and crack-free perovskite morphology during thermal aging.

Ion migration suppression in SAN-incorporated MAPI perovskite

In order to determine the structure-property relationship responsible for the enhanced thermal stability of MAPI by SAN incorporation, temperature-dependent conductivity as well as ToF-SIMS compositional depth profiling were performed. We probed the activation energy for ion migration (E_a) in pristine and SAN

incorporated MAPI films by measuring their temperature-dependent (190 K – 350 K) electrical conductance.

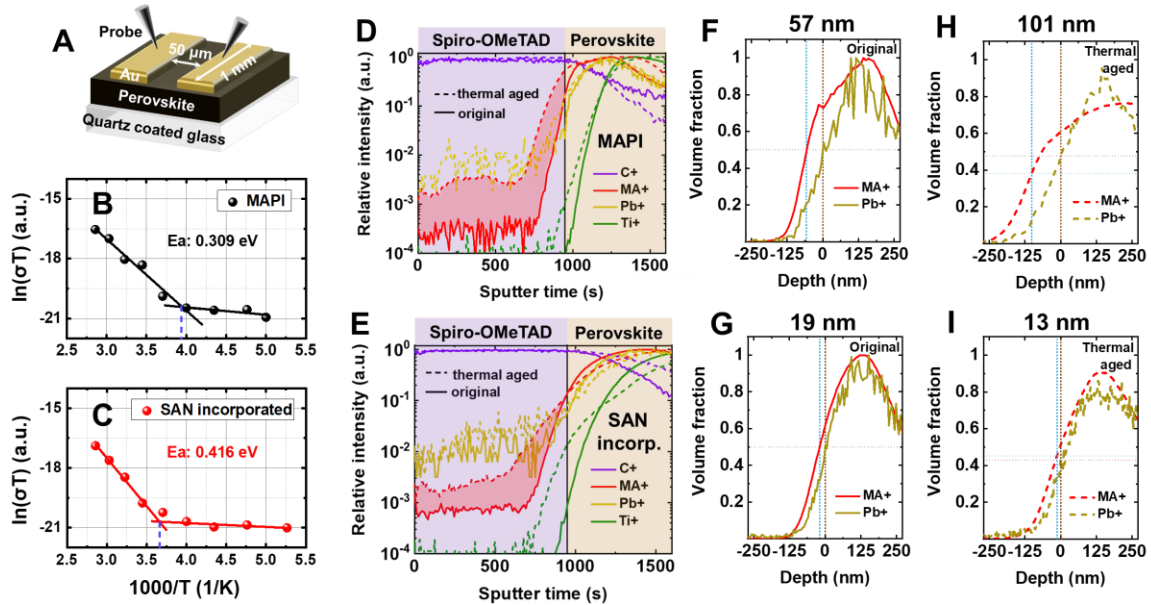


Figure 8. Ion migration characterization on the pristine and SAN-incorporated MAPI films. (A) Schematic device structure with lateral top electrode used for measuring the ion migration activation energy. (B, C) Temperature (T)-dependent conductivity (σ) of: (B) pristine and (C) SAN-incorporated MAPI films, where the slopes indicate the charge transport activation energy. (D, E) TOF-SIMS elemental depth profiles of: (D) pristine and (E) SAN-incorporated MAPI half cells before (solid) and after (dash) the thermal aging with normalized logarithmic intensities for probed elements. (F-I) The analyzed depth profiles of volume fractions of MA^+ and Pb^+ ions for (F, H) pristine and (G, I) SAN-incorporated MAPI half cells before (F, G) and after (H, I) thermal aging, respectively. Brown dashes indicate the surface of the perovskite structure, and blue dashes represent the surface of MA^+ rich components.

Two-terminal in-plane lateral electrodes with a large channel length (50 μm) (Figure 8A) help reduce the influence of electron conduction and emphasize the conduction contribution from ions during the measurements.^{9, 54} E_a was estimated by fitting the measured temperature-dependent conductivity (σ) to the Nernst-Einstein equation: $\sigma(T) = (\sigma_0/T) \exp(-E_a/kT)$, where σ_0 , T , and k denote temperature-independent pre-factor, temperature, and Boltzmann constant, respectively.^{9, 54, 65} Both pristine and SAN-incorporated perovskites feature measured $\ln(\sigma T)$ vs. $1/T$ plots with two distinctive slope (i.e., E_a) regimes (Figure

8B,C), where the lower slope in low temperature region represents mostly electron transport as most ion motion freezes out, and the higher slope in high temperature region represents ion transport. We find that the pristine and SAN-incorporated perovskite display the E_a values for ionic migration of 0.309 eV and 0.416 eV, respectively, which are comparable to what has been previously reported for pristine and polymer-added polycrystalline hybrid perovskites.^{9, 40, 54, 56, 66} The increased E_a in the SAN-incorporated perovskite clearly confirms the suppressed ion migration by the polymer additive. Consistently, the onset temperatures of ion migration (i.e., the temperatures at which the slope increases) also increases from 252.5 K in the pristine perovskite (Figure 8B) to 273.2 K in the SAN-incorporated perovskite (Figure 8C). We note that one may consider the identification of specific ionic species based on the measured E_a value, but it would be highly challenging given that there is a large variation even in the theoretically predicted E_a values for different ionic species.²² Meanwhile, the nearly identical slopes at the lower temperature region for both pristine and SAN-incorporated perovskite suggest that the SAN layer in the GB area exerts a lesser influence on the electronic transport compared with the ionic transport, which is likely caused by the much smaller size of an electron than those of the mobile ionic species in the hybrid perovskite.

Generally, the ion migration within the MAPI perovskite film is associated with the transport of iodine (I^-) and methylammonium (MA^+) ions. Between the two, it has been recently shown that the concentration of mobile MA^+ ions is one order of magnitude higher than that of mobile I^- ions²², thus mainly responsible for the accelerated degradation of MAPI at elevated temperature via the depletion of MA^+

species. We utilized the ToF-SIMS to directly determine how the SAN incorporation in the MAPI perovskite affect the MA⁺ distribution along the thickness of PSC devices before and after thermal aging. We performed the ToF-SIMS compositional depth-profiling on the pristine and SAN-incorporated MAPI half-cells, as shown in Figure 8D-I. A protective layer of Spiro-OMeTAD HTL (160 nm) was coated onto the films to preserve the structure of the MAPI perovskite film surface and simulate the interface formed in actual PSCs. The normalized ToF-SIMS spectra in Figure 8D and E show the relative intensity vs. sputtering time for C⁺ (purple), MA⁺ (red), Pb⁺ (yellow), and Ti⁺ (green) secondary ions with the traces of the original and aged films marked by solid and dashed lines, respectively. The C⁺ and Pb⁺ traces are used to delineate the approximate boundary between HTL and MAPI layers. Compared with the pristine MAPI, a larger shift of all the depth profiles towards the bottom direction, including that of Ti⁺, was observed after thermal aging in the SAN-incorporated MAPI as clearly visible in the linear-scale depth profile plots (Figure S7). This apparent broadening of the HTL/perovskite interface as well as the shift of the C⁺ trace indicate the possible accumulation of the SAN polymer at the interface as the SAN polymer is driven out of the MAPI due to the agglomeration of MAPI grains during the thermal aging.

We assume that prior to thermal treatment, the Pb⁺ trace represents the perovskite layer, and hence its FWHM is used to designate the perovskite surface (zero reference) for the depth analysis in Figure 8F-I, where the volume fractions of MA⁺ and Pb⁺ are provided before and after thermal aging as a function of depth. We find that the pristine MAPI features a 57 nm-thick layer with excessive MA⁺ formed

on the surface of the perovskite even before thermal aging, due to relatively high mobility of MA⁺ ions and their out-diffusion (Figure 8F). In contrast, the SAN-incorporated MAPI film has a much thinner MA⁺-rich surface layer (19 nm thick), indicating suppression of MA⁺ migration by the presence of the polymer even before the thermal aging. After annealing the films for 24 h at 100 °C, the thickness of MA⁺-rich layer in the pristine MAPI nearly doubles to 101 nm (Figure 8H). On the other hand, the SAN-incorporated perovskite features a slightly decreased thickness of MA⁺-rich layer (~13 nm) (Figure 8G and I), indicating no additional out-diffusion of MA⁺ after the thermal aging. These observations are consistent with the XRD results (Figure 6), which show the incorporation SAN significantly reduced the decomposition of MAPI to the PbI₂ at elevated temperatures.

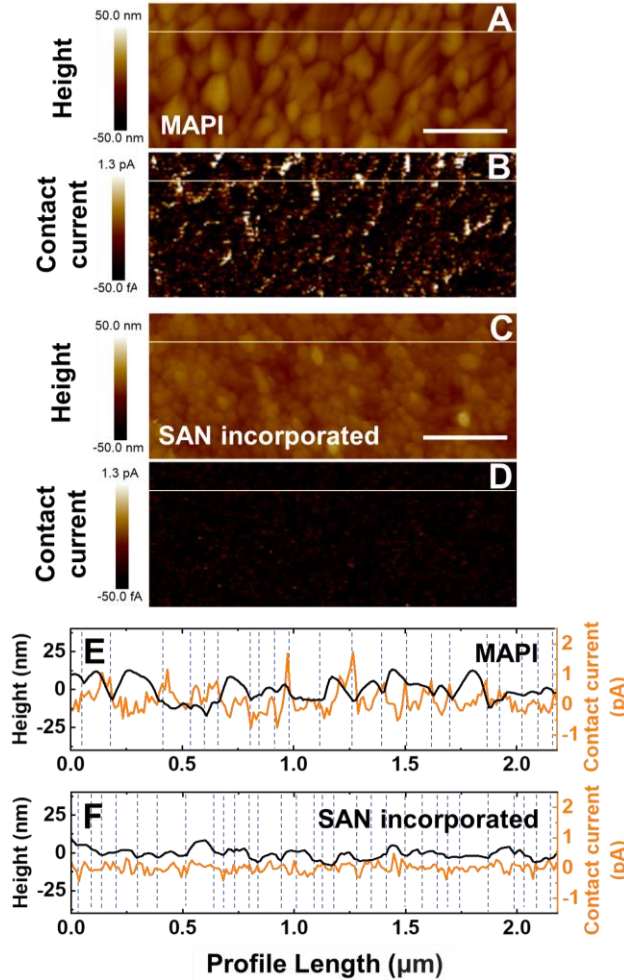


Figure 9. c-AFM data comparing height (A, C) and corresponding contact current (B, D) maps of (A, B) pristine and (C, D) SAN-incorporated MAPI films. Height (black) and contact current (orange) profiles of (E) pristine and (F) SAN-incorporated MAPI films corresponding to marked lines in A-D, the blue dashes represent GB regions. Scale bars in A and C are 500 nm.

By using c-AFM, we confirm that the ion out-diffusion primarily occurs through MAPI GB areas. The topography and contact current maps (Figure 9) were obtained by scanning the MAPI films deposited on a conductive indium tin oxide (ITO) substrate using a 20 nm-diameter Pt/Ir AFM tip. An ionic current⁶⁷ was induced in the sample by applying a 2 V bias in the vertical direction, across the ~350 nm thick film, which exerts an electrical field of ~5.7 V/ μm along the surface normal direction, much greater than the minimum value of 0.2 V/ μm previously shown to activate electrical-poling induced ion motions.⁹ Furthermore, as shown in

our E_a measurement, the mobile ions are fully activated at room temperature.^{9, 40, 54} The contact current map of the pristine MAPI film (Figure 9B) exhibits localized current signals across the images, seemingly matching the positions of GBs (Figure 9A). In a stark contrast, the SAN-incorporated MAPI does not show obvious current response (Figure 9D). Detailed height and current line profiles corresponding to the marked lines on Figure 9A-D are presented in Figure 9E and F. The result clearly shows that, in pristine MAPI, the contact current profile shows peaks around the GB areas (low height areas indicated by blue dashes), while it features a much-attenuated overall intensity with less visible peaks in the SAN-incorporated MAPI film. These observations clearly support the notion that the ion migration is dominantly facilitated by the GB areas in the pristine MAPI, and the incorporation of SAN passivates the GBs, directly suppressing the ion migration.

Discussion

Our study demonstrated the incorporation of SAN could significantly enhance the structural stability of MAPI at elevated temperature, while the surface coating of SAN on MAPI was not so effective as the thermal aging duration increased due to possible de-wetting of the ultrathin (2.8 nm) coating (Figure 3) leading to ‘break-up’ of the SAN surface. Due to the SAN thickness being drastically smaller than R_g (15.7 nm), the film de-wetting likely occurs driven by unfavorable enthalpic interaction and associated stress.⁶⁸ We find that indeed SAN has a strong interfacial tension (i.e., immiscibility) against MA⁺ in MAPI by measuring contact angle based on AFM images and considering a standard interfacial tension theory. Specifically, the interfacial tension between materials (typically polymers) is described by the Helfan-Tagami theory expressed as:⁶⁹

$$\gamma = a\rho k_B T \sqrt{\frac{\chi}{6}}$$

with γ , a , ρ , k_B , T , and χ denoting interfacial tension, statistical segment length, reciprocal of monomer volume, Boltzmann constant, temperature, the Flory-Huggins parameter, respectively. Here, except for χ and γ that measures the miscibility and interfacial tension of two materials, respectively, all other parameters can be assumed as constants for our discussion. To determine the miscibility (compatibility) between the MA⁺-rich component in MAPI and SAN, we estimated χ between MAI and SAN by experimentally measuring the contact angle of SAN on MAI and the interfacial tension between them. For the contact angle measurement, a bilayer film was prepared by first spin-casting a thick MAI film on an atomically

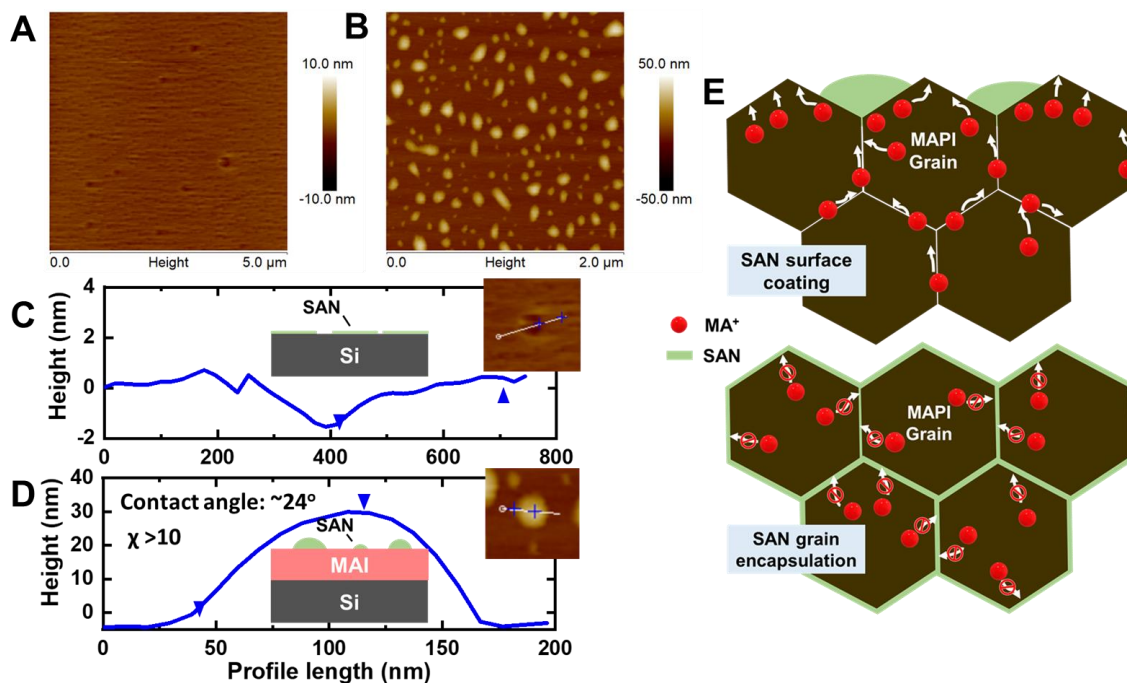


Figure 10. Miscibility measurements between MAI and SAN polymer. (A, B) AFM height images showing the dewetted morphology of an ultrathin SAN layer spun-casted on a bare Si (A) and thick MAI coated Si wafers (B), respectively, with (C, D) height profiles of specific regions shown in the insets and the schemes depicting the thin film models used for the measurements. (E) Schematic cross-sectional structure of MAPI films illustrating the migration of MA^+ ions across the untreated GBs of the SAN-surface-coated (top), and its suppression in the SAN-incorporated (bottom) MAPI films. Because highly immiscible SAN encapsulates individual grains and forms barriers at GBs suppressing the migrations of MA^+ .

flat Si wafer, followed by spin-casting of a ~ 2 nm SAN film atop. Separately, another SAN film was prepared directly on a Si wafer as a control sample. The two films were then annealed in vacuum and allowed to equilibrate. AFM topography and friction maps (Figure 10A and B) confirms that the SAN film is completely dewetted from the MAI coated surface, while only minor de-wettings with small holes are observed for the thin SAN film on Si substrate. A line profile obtained from the control SAN film on the bare Si (Figure 10C) confirms the SAN film thickness is around ~ 2 nm, while the de-wetted SAN droplet on the MAI surface (Figure 10D) has a contact angle of $\sim 24^\circ$. The observation clearly indicates high immiscibility

between MAI and SAN. Considering the measured contact angle ($\sim 24^\circ$), the dispersive component of the surface tension for SAN (0.036 J/m^2),⁷⁰ the estimated surface tension of MAI (0.2 J/m^2),⁷¹ and the Young's equation, we find that the interfacial tension γ between SAN and MAI are estimated to be $\sim 0.15 \text{ J/m}^2$, this very large surface tension is then equivalent to $\chi > 10$ based on the Helfan-Tagami equation, thus confirming that MAI and SAN are highly immiscible.

Though a further investigation would be necessary, we speculate the high immiscibility between SAN and MAI possibly results from the repulsive interaction between the cyanide group in the acrylonitrile block of SAN with MAI. Overall, the observation explains not only the observed thermal degradation of surface-SAN-coated MAPI during a prolonged thermal aging but also the superior thermal stability of directly SAN-incorporated MAPI. Particularly, as schematically illustrated in Figure 10E, in both the surface-coated and bulk-incorporated configurations, the high incompatibility between MA^+ rich components and SAN suppresses the out-diffusion MA^+ . Nevertheless, in the surface-SAN-coated MAPI, the inter-grain diffusion of MA^+ can occur across the GBs, with the ultrathin top SAN surface being prone to de-wetting under a prolonged thermal aging, eventually failing to prevent the concentrated MA^+ -rich species from out-diffusing. On the contrary, when SAN is directly incorporated in MAPI, each grain is encapsulated, with SAN geometrically confined within the GBs. This configuration is expected to be more stable against de-wetting, prevent the outward diffusion of MA^+ ions, and finally render the MA^+ ions confined within the MAPI crystal structure, enhancing its overall stability against thermal aging.

Conclusions

In this study, SAN was applied as an additive for improving the thermal stability of MAPI perovskite and its PV performance using surface coating and direct incorporation methods. XRD indicated that both methods were successful in suppressing the structural decomposition of MAPI into PbI_2 after aging at $100\text{ }^\circ\text{C}$ for 24 h, while the direct incorporation led to a much better morphological stability without the formation of cracks or pinholes unlike the surface-SAN-coated counterpart in which the high immiscibility between SAN and MA^+ was identified as likely causing the instability of SAN layer and partially exposed MAPI surface. Consistently, the thermal stability of PSC PCE was most improved by the direct SAN incorporation, exhibiting the least PCE degradation of only around 5-15% after $100\text{ }^\circ\text{C}$, 24 h thermal aging, as opposed to the 30-40% degradation of the surface-SAN-coated MAPI and over 40% of pristine MAPI. Compositional depth-profiling by ToF-SIMS and surface c-AFM measurements further confirmed that the MA^+ out-diffusion was mainly responsible for the thermal degradation of MAPI perovskite, and the incorporation of SAN suppressed the MA^+ migration along and across the GBs during thermal aging by encapsulating grains and passivating GBs. Especially, the high immiscibility between MA^+ and SAN was postulated beneficial in this case since the SAN passivating GBs would reduce both the inter-grain diffusion of MA^+ across GBs and its out-diffusion through GBs and grain surfaces. The results not only present a new class of additive specifically addressing the critical thermal stability issue of hybrid perovskites and their PV performance but

also advance the fundamental understanding associated with ion migration and the interaction of polymer additives with hybrid perovskites. The direct incorporation of SAN into hybrid perovskites also would represent a practical fabrication method that can in principle facilitate a scaled-up manufacturing of more thermally stable hybrid perovskite PV devices and systems.

Supporting Information

Table summarizing fitted lifetime parameters; Table and statistic figures of J–V characteristics; I–V curves of the perovskite with and without SAN incorporation; Lower magnification SEM image of pristine perovskite surface after thermal aging; Evolution of J–V characteristics during thermal exposure; DSC data of SAN polymer; Linear plots of TOF-SIMS results with normalized relative intensities.

Acknowledgements

The research was carried out at the Center for Functional Nanomaterials (CFN), Brookhaven National Laboratory (BNL), which is supported by the U.S. Department of Energy, Office of Basic Energy Sciences, under Contract no. DESC0012704. This work was also supported by Department of Navy award N00014-20-1-2858 issued by the Office of Naval Research. The authors acknowledge the access to the facilities at Advanced Science Research Center, the City University of New York. The authors also acknowledge the Advanced Energy Research and Technology Center (AERTC) at Stony Brook University for conductive AFM characterizations.

References

- (1) Kojima, A.; Teshima, K.; Shirai, Y.; Miyasaka, T. Organometal Halide Perovskites as Visible-Light Sensitizers for Photovoltaic Cells. *J. Am. Chem. Soc.* **2009**, *131*, 6050-1.
- (2) Jeong, M.; Choi, I. W.; Go, E. M.; Cho, Y.; Kim, M.; Lee, B.; Jeong, S.; Jo, Y.; Choi, H. W.; Lee, J.; Bae, J.-H.; Kwak, S. K.; Kim, D. S.; Yang, C. Stable Perovskite Solar Cells with Efficiency Exceeding 24.8% and 0.3-V Voltage Loss. *Science* **2020**, *369*, 1615-1620.
- (3) Idígoras, J.; Aparicio, F. J.; Contreras-Bernal, L.; Ramos-Terrón, S.; Alcaire, M.; Sánchez-Valencia, J. R.; Borrás, A.; Barranco, Á.; Anta, J. A. Enhancing Moisture and Water Resistance in Perovskite Solar Cells by Encapsulation with Ultrathin Plasma Polymers. *ACS Appl. Mater. Interfaces* **2018**, *10*, 11587-11594.
- (4) Dong, Q.; Liu, F.; Wong, M. K.; Tam, H. W.; Djurišić, A. B.; Ng, A.; Surya, C.; Chan, W. K.; Ng, A. M. C. Encapsulation of Perovskite Solar Cells for High Humidity Conditions. *ChemSusChem* **2016**, *9*, 2597-2603.
- (5) Mansour Rezaei Fumani, N.; Arabpour Roghabadi, F.; Alidaei, M.; Sadrameli, S. M.; Ahmadi, V.; Najafi, F. Prolonged Lifetime of Perovskite Solar Cells Using a Moisture-Blocked and Temperature-Controlled Encapsulation System Comprising a Phase Change Material as a Cooling Agent. *ACS Omega* **2020**, *5*, 7106-7114.
- (6) Weerasinghe, H. C.; Dkhissi, Y.; Scully, A. D.; Caruso, R. A.; Cheng, Y.-B. Encapsulation for Improving the Lifetime of Flexible Perovskite Solar Cells. *Nano Energy* **2015**, *18*, 118-125.
- (7) Kim, N.-K.; Min, Y. H.; Noh, S.; Cho, E.; Jeong, G.; Joo, M.; Ahn, S.-W.; Lee, J. S.; Kim, S.; Ihm, K.; Ahn, H.; Kang, Y.; Lee, H.-S.; Kim, D. Investigation of Thermally Induced Degradation in CH₃NH₃PbI₃ Perovskite Solar Cells using In-situ Synchrotron Radiation Analysis. *Sci. Rep.* **2017**, *7*, 4645-4645.
- (8) Guerrero, A.; You, J.; Aranda, C.; Kang, Y. S.; Garcia-Belmonte, G.; Zhou, H.; Bisquert, J.; Yang, Y. Interfacial Degradation of Planar Lead Halide Perovskite Solar Cells. *ACS Nano* **2016**, *10*, 218-24.
- (9) Xing, J.; Wang, Q.; Dong, Q.; Yuan, Y.; Fang, Y.; Huang, J. Ultrafast Ion Migration in Hybrid Perovskite Polycrystalline Thin Films under Light and Suppression in Single Crystals. *Phys. Chem. Chem. Phys.* **2016**, *18*, 30484-30490.
- (10) Leijtens, T.; Eperon, G. E.; Noel, N. K.; Habisreutinger, S. N.; Petrozza, A.; Snaith, H. J. Stability of Metal Halide Perovskite Solar Cells. *Adv. Energy Mater.* **2015**, *5*, 1500963.
- (11) Bag, M.; Renna, L. A.; Adhikari, R. Y.; Karak, S.; Liu, F.; Lahti, P. M.; Russell, T. P.; Tuominen, M. T.; Venkataraman, D. Kinetics of Ion Transport in Perovskite Active Layers and Its Implications for Active Layer Stability. *J. Am. Chem. Soc.* **2015**, *137*, 13130-7.
- (12) Nie, W.; Tsai, H.; Asadpour, R.; Blancon, J. C.; Neukirch, A. J.; Gupta, G.; Crochet, J. J.; Chhowalla, M.; Tretiak, S.; Alam, M. A.; Wang, H. L.; Mohite, A. D. Solar Cells. High-Efficiency Solution-Processed Perovskite Solar Cells with Millimeter-Scale Grains. *Science* **2015**, *347*, 522-5.
- (13) Chen, Z.; Turedi, B.; Alsalloum, A. Y.; Yang, C.; Zheng, X.; Gereige, I.; AlSaggaf, A.; Mohammed, O. F.; Bakr, O. M. Single-Crystal MAPbI₃ Perovskite Solar Cells Exceeding 21% Power Conversion Efficiency. *ACS Energy Lett.* **2019**, *4*, 1258-1259.

- (14) Quarti, C.; Mosconi, E.; Ball, J. M.; D'Innocenzo, V.; Tao, C.; Pathak, S.; Snaith, H. J.; Petrozza, A.; De Angelis, F. Structural and Optical Properties of Methylammonium Lead Iodide across the Tetragonal to Cubic Phase Transition: Implications for Perovskite Solar Cells. *Energy Environ. Sci.* **2016**, *9*, 155-163.
- (15) Caputo, M.; Cefarin, N.; Radivo, A.; Demitri, N.; Gigli, L.; Plaisier, J. R.; Panighel, M.; Di Santo, G.; Moretti, S.; Giglia, A.; Polentarutti, M.; De Angelis, F.; Mosconi, E.; Umari, P.; Tormen, M.; Goldoni, A. Electronic Structure of MAPbI₃ and MAPbCl₃: Importance of Band Alignment. *Sci. Rep.* **2019**, *9*, 15159.
- (16) Chen, Y.; He, M.; Peng, J.; Sun, Y.; Liang, Z. Structure and Growth Control of Organic-Inorganic Halide Perovskites for Optoelectronics: From Polycrystalline Films to Single Crystals. *Adv. Sci.* **2016**, *3*, 1500392.
- (17) Ava, T. T.; Al Mamun, A.; Marsillac, S.; Namkoong, G. A Review: Thermal Stability of Methylammonium Lead Halide Based Perovskite Solar Cells. *Applied Sciences* **2019**, *9*, 188.
- (18) Eperon, G. E.; Stranks, S. D.; Menelaou, C.; Johnston, M. B.; Herz, L. M.; Snaith, H. J. Formamidinium Lead Trihalide: A Broadly Tunable Perovskite for Efficient Planar Heterojunction Solar Cells. *Energy Environ. Sci.* **2014**, *7*, 982-988.
- (19) Zhang, Y.-Y.; Chen, S.; Xu, P.; Xiang, H.; Gong, X.-G.; Walsh, A.; Wei, S.-H. Intrinsic Instability of the Hybrid Halide Perovskite Semiconductor CH₃NH₃PbI₃. *Chin. Phys. Lett.* **2018**, *35*, 036104.
- (20) Zhao, Y. C.; Zhou, W. K.; Tan, H. R.; Fu, R.; Li, Q.; Lin, F.; Yu, D. P.; Walters, G.; Sargent, E. H.; Zhao, Q. Mobile -Ion-Induced Degradation of Organic Hole-Selective Layers in Perovskite Solar Cells. *J. Phys. Chem. C* **2017**, *121*, 14517-14523.
- (21) Ma, L.; Guo, D.; Li, M.; Wang, C.; Zhou, Z.; Zhao, X.; Zhang, F.; Ao, Z.; Nie, Z. Temperature-Dependent Thermal Decomposition Pathway of Organic-Inorganic Halide Perovskite Materials. *Chem. Mater.* **2019**, *31*, 8515-8522.
- (22) Futscher, M. H.; Lee, J. M.; McGovern, L.; Muscarella, L. A.; Wang, T.; Haider, M. I.; Fakharuddin, A.; Schmidt-Mende, L.; Ehrler, B. Quantification of Ion Migration in CH₃NH₃PbI₃ Perovskite Solar Cells by Transient Capacitance Measurements. *Mater. Horiz.* **2019**, *6*, 1497-1503.
- (23) Yin, W. J.; Shi, T.; Yan, Y. Unique Properties of Halide Perovskites as Possible Origins of the Superior Solar Cell Performance. *Adv. Mater.* **2014**, *26*, 4653-8.
- (24) Chen, J.; Lee, D.; Park, N. G. Stabilizing the Ag Electrode and Reducing J-V Hysteresis through Suppression of Iodide Migration in Perovskite Solar Cells. *ACS Appl. Mater. Interfaces* **2017**, *9*, 36338-36349.
- (25) Shao, Y. C.; Fang, Y. J.; Li, T.; Wang, Q.; Dong, Q. F.; Deng, Y. H.; Yuan, Y. B.; Wei, H. T.; Wang, M. Y.; Gruverman, A.; Shialda, J.; Huang, J. S. Grain Boundary Dominated Ion Migration in Polycrystalline Organic-Inorganic Halide Perovskite Films. *Energy Environ. Sci.* **2016**, *9*, 1752-1759.
- (26) Yi, C.; Luo, J.; Meloni, S.; Boziki, A.; Ashari-Astani, N.; Grätzel, C.; Zakeeruddin, S. M.; Röthlisberger, U.; Grätzel, M. Entropic Stabilization of Mixed A-Cation ABX₃ Metal Halide Perovskites for High Performance Perovskite Solar Cells. *Energy Environ. Sci.* **2016**, *9*, 656-662.
- (27) Zhou, W.; Zhao, Y.; Zhou, X.; Fu, R.; Li, Q.; Zhao, Y.; Liu, K.; Yu, D.; Zhao, Q. Light-Independent Ionic Transport in Inorganic Perovskite and Ultrastable Cs-Based Perovskite Solar Cells. *J. Phys. Chem. Lett.* **2017**, *8*, 4122-4128.

- (28) Kennard, R. M.; Dahlman, C. J.; Nakayama, H.; DeCrescent, R. A.; Schuller, J. A.; Seshadri, R.; Mukherjee, K.; Chabynyc, M. L. Phase Stability and Diffusion in Lateral Heterostructures of Methyl Ammonium Lead Halide Perovskites. *ACS Appl. Mater. Interfaces* **2019**, *11*, 25313-25321.
- (29) Rybin, N.; Ghosh, D.; Tisdale, J.; Shrestha, S.; Yoho, M.; Vo, D.; Even, J.; Katan, C.; Nie, W.; Neukirch, A. J.; Tretiak, S. Effects of Chlorine Mixing on Optoelectronics, Ion Migration, and Gamma-Ray Detection in Bromide Perovskites. *Chem. Mater.* **2020**, *32*, 1854-1863.
- (30) Wei, H.; Chen, S.; Zhao, J.; Yu, Z.; Huang, J. Is Formamidinium Always More Stable than Methylammonium? *Chem. Mater.* **2020**, *32*, 2501-2507.
- (31) Dou, B.; Wheeler, L. M.; Christians, J. A.; Moore, D. T.; Harvey, S. P.; Berry, J. J.; Barnes, F. S.; Shaheen, S. E.; van Hest, M. F. A. M. Degradation of Highly Alloyed Metal Halide Perovskite Precursor Inks: Mechanism and Storage Solutions. *ACS Energy Lett.* **2018**, *3*, 979-985.
- (32) Gedamu, D.; Asuo, I. M.; Benetti, D.; Basti, M.; Ka, I.; Cloutier, S. G.; Rosei, F.; Nechache, R. Solvent-Antisolvent Ambient Processed Large Grain Size Perovskite Thin Films for High-Performance Solar Cells. *Sci. Rep.* **2018**, *8*, 12885.
- (33) Tsai, H.; Nie, W.; Cheruku, P.; Mack, N. H.; Xu, P.; Gupta, G.; Mohite, A. D.; Wang, H.-L. Optimizing Composition and Morphology for Large-Grain Perovskite Solar Cells via Chemical Control. *Chem. Mater.* **2015**, *27*, 5570-5576.
- (34) Jiang, Q.; Zhao, Y.; Zhang, X.; Yang, X.; Chen, Y.; Chu, Z.; Ye, Q.; Li, X.; Yin, Z.; You, J. Surface Passivation of Perovskite Film for Efficient Solar Cells. *Nat. Photonics* **2019**, *13*, 460-466.
- (35) Hadadian, M.; Correa-Baena, J.-P.; Goharshadi, E. K.; Ummadisingu, A.; Seo, J.-Y.; Luo, J.; Gholipour, S.; Zakeeruddin, S. M.; Saliba, M.; Abate, A.; Grätzel, M.; Hagfeldt, A. Enhancing Efficiency of Perovskite Solar Cells via N-doped Graphene: Crystal Modification and Surface Passivation. *Adv. Mater.* **2016**, *28*, 8681-8686.
- (36) Li, M.; Yan, X.; Kang, Z.; Huan, Y.; Li, Y.; Zhang, R.; Zhang, Y. Hydrophobic Polystyrene Passivation Layer for Simultaneously Improved Efficiency and Stability in Perovskite Solar Cells. *ACS Appl. Mater. Interfaces* **2018**, *10*, 18787-18795.
- (37) Peng, J.; Khan, J. I.; Liu, W.; Ugur, E.; Duong, T.; Wu, Y.; Shen, H.; Wang, K.; Dang, H.; Aydin, E.; Yang, X.; Wan, Y.; Weber, K. J.; Catchpole, K. R.; Laquai, F.; De Wolf, S.; White, T. P. A Universal Double-Side Passivation for High Open-Circuit Voltage in Perovskite Solar Cells: Role of Carbonyl Groups in Poly(methyl methacrylate). *Adv. Energy Mater.* **2018**, *8*, 1801208.
- (38) Niu, T.; Lu, J.; Munir, R.; Li, J.; Barrit, D.; Zhang, X.; Hu, H.; Yang, Z.; Amassian, A.; Zhao, K.; Liu, S. F. Stable High-Performance Perovskite Solar Cells via Grain Boundary Passivation. *Adv. Mater.* **2018**, *30*, 1706576.
- (39) Hou, X.; Huang, S.; Ou-Yang, W.; Pan, L.; Sun, Z.; Chen, X. Constructing Efficient and Stable Perovskite Solar Cells via Interconnecting Perovskite Grains. *ACS Appl. Mater. Interfaces* **2017**, *9*, 35200-35208.
- (40) Zhou, Y.; Yin, Y.; Zuo, X.; Wang, L.; Li, T.-D.; Zhou, Y.; Padture, N. P.; Yang, Z.; Guo, Y.; Xue, Y.; Kisslinger, K.; Cotlet, M.; Nam, C.-Y.; Rafailovich, M. H. Enhancing Chemical Stability and Suppressing Ion Migration in CH₃NH₃PbI₃ Perovskite Solar Cells via Direct Backbone Attachment of Polyesters on Grain Boundaries. *Chem. Mater.* **2020**, *32*, 5104-5117.

- (41) Wang, C.; Song, Z.; Zhao, D.; Awni, R. A.; Li, C.; Shrestha, N.; Chen, C.; Yin, X.; Li, D.; Ellingson, R. J.; Zhao, X.; Li, X.; Yan, Y. Improving Performance and Stability of Planar Perovskite Solar Cells through Grain Boundary Passivation with Block Copolymers. *Sol. RRL* **2019**, *3*, 1900078.
- (42) Zong, Y. X.; Zhou, Y. Y.; Zhang, Y.; Li, Z. P.; Zhang, L.; Ju, M. G.; Chen, M.; Pang, S. P.; Zeng, X. C.; Padture, N. P. Continuous Grain-Boundary Functionalization for High-Efficiency Perovskite Solar Cells with Exceptional Stability. *Chem* **2018**, *4*, 1404-1415.
- (43) Liu, T.; Zhou, Y.; Li, Z.; Zhang, L.; Ju, M.-G.; Luo, D.; Yang, Y.; Yang, M.; Kim, D. H.; Yang, W.; Padture, N. P.; Beard, M. C.; Zeng, X. C.; Zhu, K.; Gong, Q.; Zhu, R. Stable Formamidinium-Based Perovskite Solar Cells via In Situ Grain Encapsulation. *Adv. Energy Mater.* **2018**, *8*, 1800232.
- (44) Huang, Z.; Hu, X.; Liu, C.; Tan, L.; Chen, Y. Nucleation and Crystallization Control via Polyurethane to Enhance the Bendability of Perovskite Solar Cells with Excellent Device Performance. *Adv. Funct. Mater.* **2017**, *27*, 1703061.
- (45) Lin, H.-S.; Okawa, S.; Ma, Y.; Yotsumoto, S.; Lee, C.; Tan, S.; Manzhos, S.; Yoshizawa, M.; Chiashi, S.; Lee, H. M.; Tanaka, T.; Kataura, H.; Jeon, I.; Matsuo, Y.; Maruyama, S. Polyaromatic Nanotweezers on Semiconducting Carbon Nanotubes for the Growth and Interfacing of Lead Halide Perovskite Crystal Grains in Solar Cells. *Chem. Mater.* **2020**, *32*, 5125-5133.
- (46) Wang, Y.; Zhou, Y.; Zhang, T.; Ju, M.-G.; Zhang, L.; Kan, M.; Li, Y.; Zeng, X. C.; Padture, N. P.; Zhao, Y. Integration of A Functionalized Graphene Nano-Network into A Planar Perovskite Absorber for High-Efficiency Large-Area Solar Cells. *Mater. Horiz.* **2018**, *5*, 868-873.
- (47) Li, B.; Fei, C.; Zheng, K.; Qu, X.; Pullerits, T.; Cao, G.; Tian, J. Constructing Water-Resistant $\text{CH}_3\text{NH}_3\text{PbI}_3$ Perovskite Films via Coordination Interaction. *J. Mater. Chem. A* **2016**, *4*, 17018-17024.
- (48) Bi, D. Q.; Yi, C. Y.; Luo, J. S.; Decoppet, J. D.; Zhang, F.; Zakeeruddin, S. M.; Li, X.; Hagfeldt, A.; Gratzel, M. Polymer-Templated Nucleation and Crystal Growth of Perovskite Films for Solar Cells with Efficiency Greater than 21%. *Nat. Energy* **2016**, *1*, 16142.
- (49) Guo, Y.; Shoyama, K.; Sato, W.; Nakamura, E. Polymer Stabilization of Lead(II) Perovskite Cubic Nanocrystals for Semitransparent Solar Cells. *Adv. Energy Mater.* **2016**, *6*, 1502317.
- (50) Sun, Y.; Wu, Y.; Fang, X.; Xu, L.; Ma, Z.; Lu, Y.; Zhang, W.-H.; Yu, Q.; Yuan, N.; Ding, J. Long-Term Stability of Organic-Inorganic Hybrid Perovskite Solar Cells with High Efficiency under High Humidity Conditions. *J. Mater. Chem. A* **2017**, *5*, 1374-1379.
- (51) Zhang, C.-C.; Li, M.; Wang, Z.-K.; Jiang, Y.-R.; Liu, H.-R.; Yang, Y.-G.; Gao, X.-Y.; Ma, H. Passivated Perovskite Crystallization and Stability in Organic-Inorganic Halide Solar Cells by Doping A Donor Polymer. *J. Mater. Chem. A* **2017**, *5*, 2572-2579.
- (52) Zhao, W.; Rafailovich, M. H.; Sokolov, J.; Fetters, L. J.; Plano, R.; Sanyal, M. K.; Sinha, S. K.; Sauer, B. B. Wetting Properties of Thin Liquid Polyethylene Propylene Films. *Phys. Rev. Lett.* **1993**, *70*, 1453-1456.
- (53) de Gennes, P. G. Wetting: Statics and Dynamics. *Rev. Mod. Phys.* **1985**, *57*, 827-863.

- (54) Li, X.; Zhang, W.; Wang, Y. C.; Zhang, W.; Wang, H. Q.; Fang, J. In-Situ Cross-Linking Strategy for Efficient and Operationally Stable Methylammonium Lead Iodide Solar Cells. *Nat. Commun.* **2018**, *9*, 3806.
- (55) Shi, D.; Adinolfi, V.; Comin, R.; Yuan, M.; Alarousu, E.; Buin, A.; Chen, Y.; Hoogland, S.; Rothenberger, A.; Katsiev, K.; Losovyj, Y.; Zhang, X.; Dowben, P. A.; Mohammed, O. F.; Sargent, E. H.; Bakr, O. M. Low Trap-State Density and Long Carrier Diffusion in Organolead Trihalide Perovskite Single Crystals. *Science* **2015**, *347*, 519.
- (56) Han, T. H.; Lee, J. W.; Choi, C.; Tan, S.; Lee, C.; Zhao, Y.; Dai, Z.; De Marco, N.; Lee, S. J.; Bae, S. H.; Yuan, Y.; Lee, H. M.; Huang, Y.; Yang, Y. Perovskite-Polymer Composite Cross-Linker Approach for Highly-Stable and Efficient Perovskite Solar Cells. *Nat. Commun.* **2019**, *10*, 520.
- (57) Kim, H.-S.; Park, N.-G. Parameters Affecting I–V Hysteresis of CH₃NH₃PbI₃ Perovskite Solar Cells: Effects of Perovskite Crystal Size and Mesoporous TiO₂ Layer. *J. Phys. Chem. Lett.* **2014**, *5*, 2927-2934.
- (58) Zhang, T.; Chen, H.; Bai, Y.; Xiao, S.; Zhu, L.; Hu, C.; Xue, Q.; Yang, S. Understanding the Relationship between Ion Migration and the Anomalous Hysteresis in High-Efficiency Perovskite Solar Cells: A Fresh Perspective from Halide Substitution. *Nano Energy* **2016**, *26*, 620-630.
- (59) Chen, B.; Yu, Z.; Liu, K.; Zheng, X.; Liu, Y.; Shi, J.; Spronk, D.; Rudd, P. N.; Holman, Z.; Huang, J. Grain Engineering for Perovskite/Silicon Monolithic Tandem Solar Cells with Efficiency of 25.4%. *Joule* **2019**, *3*, 177-190.
- (60) Saliba, M.; Etgar, L. Current Density Mismatch in Perovskite Solar Cells. *ACS Energy Lett.* **2020**, *5*, 2886-2888.
- (61) Christians, J. A.; Manser, J. S.; Kamat, P. V. Best Practices in Perovskite Solar Cell Efficiency Measurements. Avoiding the Error of Making Bad Cells Look Good. *J. Phys. Chem. Lett.* **2015**, *6*, 852-857.
- (62) Ciccio, A.; Latini, A. Thermodynamics and the Intrinsic Stability of Lead Halide Perovskites CH₃NH₃PbX₃. *J. Phys. Chem. Lett.* **2018**, *9*, 3756-3765.
- (63) Wang, T.; Lian, G.; Huang, L.; Zhu, F.; Cui, D.; Wang, Q.; Meng, Q.; Jiang, H.; Zhou, G.; Wong, C.-P. A Crystal-Growth Boundary-Fusion Strategy to Prepare High-Quality MAPbI₃ Films for Excellent Vis-NIR Photodetectors. *Nano Energy* **2019**, *64*, 103914.
- (64) Roose, B.; Ummadisingu, A.; Correa-Baena, J.-P.; Saliba, M.; Hagfeldt, A.; Graetzel, M.; Steiner, U.; Abate, A. Spontaneous Crystal Coalescence Enables Highly Efficient Perovskite Solar Cells. *Nano Energy* **2017**, *39*, 24-29.
- (65) Bischoff, C.; Schuller, K.; Beckman, S. P.; Martin, S. W. Non-Arrhenius Ionic Conductivities in Glasses due to A Distribution of Activation Energies. *Phys. Rev. Lett.* **2012**, *109*, 075901.
- (66) Lee, J.-W.; Dai, Z.; Han, T.-H.; Choi, C.; Chang, S.-Y.; Lee, S.-J.; De Marco, N.; Zhao, H.; Sun, P.; Huang, Y.; Yang, Y. 2D Perovskite Stabilized Phase-Pure Formamidinium Perovskite Solar Cells. *Nat. Commun.* **2018**, *9*, 3021.
- (67) Hoque, M. N. F.; He, R.; Warzywoda, J.; Fan, Z. Effects of Moisture-Based Grain Boundary Passivation on Cell Performance and Ionic Migration in Organic–Inorganic Halide Perovskite Solar Cells. *ACS Appl. Mater. Interfaces* **2018**, *10*, 30322-30329.
- (68) Clarke, C. J.; Eisenberg, A.; La Scala, J.; Rafailovich, M. H.; Sokolov, J.; Li, Z.; Qu, S.; Nguyen, D.; Schwarz, S. A.; Strzhemechny, Y.; Sauer, B. B. Measurements of the

Flory–Huggins Interaction Parameter for Polystyrene–Poly(4-vinylpyridine) Blends. *Macromolecules* **1997**, *30*, 4184-4188.

(69) Helfand, E.; Tagami, Y. Theory of the Interface Between Immiscible Polymers. *J. Chem. Phys.* **1972**, *57*, 1812-1813.

(70) Mehrabi Mazidi, M.; Edalat, A.; Berahman, R.; Hosseini, F. S. Highly-Toughened Polylactide- (PLA-) Based Ternary Blends with Significantly Enhanced Glass Transition and Melt Strength: Tailoring the Interfacial Interactions, Phase Morphology, and Performance. *Macromolecules* **2018**, *51*, 4298-4314.

(71) Li, B.; Isikgor, F. H.; Coskun, H.; Ouyang, J. The Effect of Methylammonium Iodide on the Supersaturation and Interfacial Energy of the Crystallization of Methylammonium Lead Triiodide Single Crystals. *Angew. Chem. Int. Ed.* **2017**, *56*, 16073-16076.

TOC Figure

